A Dissertation for the Degree of Doctor of Philosophy

Targeting Macrophages in the Microenvironment of Inflammation and Cancer

염증 및 종양 미세환경에서 큰포식세포 표적화 연구

By

Juha Song, D.V.M.

August 2020

College of Veterinary Medicine

Department of Veterinary Pathology and Preventive Medicine

(Laboratory Animal Medicine)

Graduate School of Seoul National University

`

Targeting Macrophages in the Microenvironment of Inflammation and Cancer

염증 및 종양 미세환경에서 큰포식세포 표적화 연구

By

Juha Song, D.V.M.

August 2020

College of Veterinary Medicine

Department of Veterinary Pathology and Preventive Medicine

(Laboratory Animal Medicine)

Graduate School of Seoul National University

`

1. ABSTRACT

Macrophages are highly abundant in cancer- and inflammatory-associated microenvironments, and their presence at the site of disease modulates these microenvironments towards disease-favorable conditions. Tissue-resident macrophages adapt to their surroundings, allowing them to perform functions specific to their local microenvironment. For this reason, macrophages should be analyzed and targeted in the context of the disease-specific microenvironment. In this study, I aimed to examine the microenvironmental changes in choroidal neovascularization (CNV), an inflammatory eye disease, and in ovarian cancer. I sought to investigate the characteristics of the infiltrating macrophages, based on which I suggest strategies for the development of therapeutic interventions. Herein, I have revealed that inflammation beyond homeostasis-maintaining parainflammation in the retinal pigment epithelium (RPE) results in the suppression of mitochondrial metabolism and perturbations of glucose, lipid, and amino acid metabolic pathways. Indeed, for the first time, I was able to demonstrate increased lactic acid levels in the RPE-choroid complex in an experimentally-induced CNV mouse model. Lactic acid, a glycolytic end-product, facilitated neovascularization by enhancing the pro-angiogenic properties of the infiltrating macrophage population. Blocking lactic acid signaling in macrophages significantly reduced CNV, suggesting that it is a promising strategy for future CNV treatment (Chapter 1). Next, using a zebrafish tumor metastasis model, I also found that substantial numbers of macrophages were recruited to areas surrounding the ovarian cancer cells implanted. Monocytes

`

recruitment, macrophage activation, and interaction with cancer cells during early dissemination were significantly enhanced through the factor inhibiting HIF (FIH)－G9a signaling axis in ovarian cancer cells. Indeed, secretome analysis of cancer－derived supernatants revealed an overall upregulation of cytokines, such as transforming growth factor β1 (TGFβ1) and vascular endothelial growth factor A (VEGFA), fostering a pro－tumorigenic and pro－metastatic tumor microenvironment. Based on a reliable model, I have also developed a potential therapeutic strategy that can block cancer intravasation and metastasis (Chapter 2). Together, my results provide valuable insight into the disease mechanisms in inflammatory disease and cancer research, paving the way for future mechanistic studies.

`

2. GENERAL INTRODUCTION

The microenvironment in a variety of disease states is influenced by both pathological processes and a patient's overall health status [1]. Initiation of changes at the microenvironmental level can have both local and systemic implications [2]. Consequently, it is critical to understand the various models of disease microenvironments and their potential consequences so as to appropriately diagnose the disease, and fine-tune the treatment strategy accordingly [1]. Typically, when thinking of pathological processes that have a strong microenvironmental component, cancer and chronic inflammatory diseases, such as arthritis, stand out. Associated microenvironments show similar tendencies of being pathologically driven by inflammation, thereby sharing common characteristics among the encapsulated microenvironments [1].

Macrophages are highly abundant in cancer- and inflammatory-associated microenvironments, and their presence at the site of disease modulates these microenvironments towards disease-favorable conditions. [3]. In fact, although "macrophage activation" is the term commonly used in this context, however, numerous experimental evidences have shown that this activated phenotype is highly dynamic, depending on the stimulus driving recruitment and activation, and the corresponding locations where these processes are initiated [4]. The phenotypic heterogeneity of macrophages generated in vitro coincides with the wide array of phenotypes that occur in vivo [5]. Tissue-resident macrophages adapt to their surroundings, allowing them to perform functions specific to their local microenvironment [3, 5]. For this reason,

`

macrophages should be analyzed and targeted in the context of the disease—specific microenvironment.

In this study, I aimed to unravel the microenvironmental changes facilitating the pathological progression of choroidal neovascularization (CNV), an inflammatory eye disease, and of ovarian cancer. I sought to analyze the characteristics of the infiltrating macrophages, based on which I suggest strategies for the development of therapeutic interventions. First, using the latest proteome and phosphoproteome profiling approaches, I was able to reveal that inflammation beyond homeostasis—maintaining parainflammation in the retinal pigment epithelium (RPE) results in the suppression of mitochondrial metabolism and perturbations of glucose, lipid, and amino acid metabolism pathways. Accordingly, I was able to detect increased lactic acid levels in the RPE—choroid complex in an experimentally—induced CNV mouse model. Lactic acid, a glycolytic end—product, facilitated neovascularization by enhancing the pro—angiogenic properties of infiltrating macrophage population. Blocking lactic acid signaling in macrophages significantly reduced CNV, suggesting that it is a promising strategy for future CNV treatment. Next, using a zebrafish tumor metastasis model, I also found that substantial numbers of macrophages were recruited to areas surrounding the ovarian cancer cells implanted. Monocytes recruitment, macrophage activation, and interaction with cancer cells during early dissemination were significantly enhanced through the FIH—G9a signaling axis in ovarian cancer cells. Indeed, secretome analysis of cancer—derived supernatants revealed an overall upregulation of cytokines, such as transforming growth factor $\beta 1$ (TGF$\beta 1$) and vascular endothelial growth factor A (VEGFA), fostering a pro—

`

tumorigenic and pro-metastatic tumor microenvironment. Based on a reliable model, I have also developed a potential therapeutic strategy that can block cancer intravasation and metastasis. Together, my results provide valuable insight into the disease mechanisms in inflammatory disease and cancer research, paving the way for future mechanistic studies.

`

3. CONTENTS

4. LIST OF TABLES AND FIGURES

CHAPTER 1. Finding a Macrophage Targeting Strategy in Inflammatory

Disease

`

CHAPTER 2. Finding a Macrophage Targeting Strategy in Cancer

`

5. LIST OF ABBREVIATIONS

RPE: retinal pigment epithelium

AMD: age-related macular degeneration

CNV: choroidal neovascularization

BrM: Bruch's membrane

MCT: monocarboxylate transporter

VEGF: vascular endothelial growth factor

LA: lactic acid

IB4: isolectin B4

MFI: mean fluorescence intensity

TMT: tandem-mass tag

LPS: lipopolysaccharide

α-CHC: alpha-cyanohydroxycinnamic acid

ECAR: extracellular acidification rate

OCR: oxygen consumption rate

FDR: false discovery rate

PCA: principal component analysis

DEP: differentially expressed protein

DPP: differentially phosphorylated protein

HCL: hierarchical clustering

GSEA: gene set enrichment analysis

ER: endoplasmic reticulum

`

GO: gene ontology

HIF1α: hypoxia-inducible factor 1α

ICAM-1: intracellular adhesion molecule 1

OXPHOS: oxidative phosphorylation

PMA: 12-myristate 13-acetate

FIH: factor inhibiting HIF

TAM: tumor-associated macrophage

EMT: epithelial-to-mesenchymal transition

PVS: perivitelline space

CM: conditioned media

BMDM: bone marrow-derived macrophage

Tg: transgenic

MO: morpholino

PDGFC: platelet-derived growth factor C

FGF: fibroblast growth factor

MMP: matrix metalloproteinase

iNOS: inducible NO synthase

`

6. CHAPTER 1

Finding a Macrophage Targeting Strategy in Inflammatory Disease

; Lactic acid upregulates VEGF expression in macrophages and facilitates choroidal neovascularization

`

6.1. INTRODUCTION

The RPE is a hexagonal pigmented cell layer located between the retina and choroid [6]. As part of blood-ocular barrier, the RPE helps maintain retinal homeostasis and visual function through mutualistic physical and metabolic interactions with the retina, and supports immune privilege by producing cell-surface and soluble inhibitory molecules such as CD86 and TGFβ [7-10]. Perturbations caused by aging, genetic predisposition, or environmental insults result in a wide range of retinal dystrophies such as age-related macular degeneration (AMD) [11, 12]. Importantly, many studies have noted that the allostatic overload imposed during RPE pathogenesis results in inflammation [13-15]. Although low-grade para-inflammation exerts a cytoprotective effect against local stress, overwhelming and persistent inflammatory processes caused by complex biological disturbances, such as oxidative stress, complement abnormalities, and drusenoid dsposits, are known to instigate the recruitment and activation of immune cells, exacerbating metabolic and pathobiological changes to the RPE [15]. However, the precise mechanisms causing these destructive changes to the RPE remain unclear. An improved understanding of RPE-specific inflammatory responses that determine disease progression is necessary.

CNV, a wet form of AMD, is a leading cause of visual impairment and legal blindness in people older than 50 years [11]. Newly formed blood vessels extend anteriorly through breaks in Bruch's membrane and invade the subretinal space, resulting in hemorrhage, fluid exudation, and, eventually, photoreceptor degeneration [16]. Experimental data suggest that CNV results

14

`

from responses of the RPE to heterogeneous stressors, including aging, smoking, or genetic predisposition, creating microenvironments that promote abnormal neovascularization [17]. A number of efforts have been undertaken to discover reliable indicators of CNV development. Of note, recent findings suggest that an assessment of altered metabolic states could be a comprehensive means for identifying CNV progression. However, few studies have evaluated the metabolic influence on CNV pathogenesis [18−22].

The high−sensitivity tandem mass tag (TMT) labeling approach coupled with high−resolution mass spectrometry is a recently developed proteome technique that can identify thousands of proteins with improved coverage and accuracy [23]. In this study, by employing a TMT label−based quantitative approach using the human RPE cell line ARPE−19, I sought to elucidate differential expression patterns in the proteome and phosphoproteome of ARPE−19 cells exposed to lipopolysaccharide (LPS) compared to control cells. By doing so, I aimed to identify how aberrant pathways induce the RPE degeneration phenotype. After choosing a promising target metabolite expected to be involved in the pathobiology, I evaluated its value as a therapeutic target using an in vivo laser−induced CNV mouse model. Here, I demonstrate that lactic acid levels were significantly increased in laser−induced CNV mice. Through in vitro and in vivo studies, lactic acid was found to serve as a pro−angiogenic agent by increasing the VEGF content of macrophages, but not that of other surrounding cells. This was effectively inhibited by blocking of lactic acid uptake through treatment with the monocarboxylate transporter 1 (MCT1) blocker, α−cyanohydroxycinnamic acid (α−CHC). Finally, α−CHC−injected CNV mice showed significantly

15

`

reduced neovascular lesions compared with vehicle-treated mice. Thus, blockade of lactic acid signaling in macrophages may have anti-angiogenic effects and should thus be considered for future therapeutic application in CNV.

`

6.2. MATERIALS AND METHODS

Cell Line Culture and Reagents

Human ARPE-19 cells were purchased from the ATCC (CRL-2302, Manassas, VA, USA) and cultured in Dulbecco's modified essential medium and Ham's F12 (DMEM/F12, 1:1, Gibco, Carlsbad, CA, USA) supplemented with 10% fetal bovine serum (FBS, Gibco), 2 mM L-glutamine (Gibco), and 1% penicillin-streptomycin (Gibco) at 37 ℃ under 5% CO^2 in a humidified incubator. For proteomic and phosphoproteomic analysis, cells were seeded onto a 100-mm dish tissue culture plate (3.5×10^6 cells per well; Corning GlassWorks, Corning, NY, USA) and differentiated in DMEM/F12 media with reduced serum (1% FBS) for 7 days. For in vitro experiment, cells were seeded in 24-well tissue culture plates (1.5×10^5 cells per well; Corning GlassWorks) and maintained for 7 days. The culture medium was changed every 2 days. Polarized monolayer cultures showing TEER greater than 40 Ωcm2 were used for the downstream experiments. Human umbilical vein endothelial cells (HUVECs; Lonza Ltd., Basel, Switzerland) were purchased and cultured in endothelial growth medium-2 (EGM-2) (Lonza). Human acute monocytic leukemia THP-1 cell line was maintained in RPMI media containing 10% FBS (Gibco). Differentiation of THP-1 cells into macrophages was performed by incubation with 15 ng/mL phorbol 12-myristate 13-acetate (PMA) (Sigma-Aldrich Corp., St. Louis, MO, USA) for 2 days at 37℃ with 5% CO_2.

Immunofluorescence Staining

`

After fixed with 4% paraformaldehyde for 15 min at room temperature, ARPE-19 cells were washed with PBS containing 0.3% Triton X-100 (PBST) three times and blocked at 37 °C for 1 h in PBST supplemented with 5% FBS (Gibco). Then, the cells were incubated with the following primary antibodies at 4℃ overnight: rabbit anti-ZO-1 (Santa Cruz Biotechnology Inc., Santa Cruz, CA, USA), mouse anti-Na$^+$K$^+$ATPase (Santa Cruz Biotechnology Inc.), and mouse anti-RPE-65 (Novus Biologicals, Littleton, CO, USA). Cells were washed 3 times for 5 min with PBST and incubated with Alexa Fluor 488-labeled goat anti-rabbit IgG (Molecular Probes, Eugene, OR, USA) and Alexa Fluor 635-labeled goat anti-mouse IgG (Molecular Probes) for 1 h at room temperature. Stained cells were examined under Olympus FV1000 Confocal Scanning Scope (Olympus, Tokyo, Japan).

Sample Preparation for Proteomic and Phosphoproteomic analysis

ARPE-19 cells were stimulated with different concentrations of LPS (from *Salmonella enteritidis*, Sigma) for the indicated periods (45 min and 24 h; n = 3). Unchallenged cells (denoted as 0 min) were used as controls. Then, LPS-treated and control ARPE-19 cells were immediately washed twice and harvested with 1 mL of ice-cold PBS containing protease inhibitor and phosphatase inhibitor (GenDepot, Barker, TX, USA). Cells were stored at −80℃ for the downstream proteomic and phosphoproteomic analysis.

Protein Digestion

Cell lysates were digested using the Filter Aided Sample Preparation (FASP) method [24, 25]. First, cell pellets were lysed with the lysis buffer (4% SDS,

`

1 mM DTT, and 0.1 M HEPES pH 7.5). Protein concentration was determined using the BCA reducing compatible kit (Thermo Fisher Scientific, Rockford, IL, USA). After acetone precipitation with 200 μg of protein, pellets were resolved with the SDT buffer (4% SDS, 2 mM TCEP, and 10 mM CAA in 0.1 M HEPES, pH 7.5) and heated on a heat block at 95℃ for 15 min. Samples were then mixed with 200 μL of UA solution (8 M UREA in 0.1 M HEPES, pH 7.5). Next, the samples were subjected to a 30 kDa Amicon Ultracel filter (Millipore, Burlington, MA, USA) and centrifuged at 14,000 × g for 15 min. After two buffer exchanges with UA solution, further buffer exchanges were performed with 40 mM of HEPES pH 7.5 three times. Protein digestion was performed overnight at 37℃ using a trypsin/LysC mixture at a 100:1 protein to enzyme ratio (w/w). Peptides were collected by centrifugation.

TMT 10-Plex Labeling

Before TMT labeling, the peptide concentration of each sample was measured using a tryptophan assay [26]. TMT 10-plex labeling was then performed with some modifications to the manufacturer's protocol [24]. Peptides were labeled with TMT 10-plex reagents, such that peptides from control replicates were conjugated to tags 126, 127N, and 127C, LPS treated (45 min) replicates with tags 128N, 128C, and 129N, and LPS treated (24 h) replicates with tags 129C, 130N, and 130C, then pooled sample with tag 131. The TMT reagent that dissolved in 100% of acetonitrile (ACN) was added to 300 μg of peptide along with ACN to give a final concentration of 30% v/v. After incubation at room temperature for 1 h, the TMT-labeled samples were pooled at a 1:1:1:1:1:1:1:1:1:1 ratio. The pooled sample was dried almost

19

`

completely and desalted using a C18 solid-phase extraction (SPE) column (Waters).

High-pH Peptide Fractionation

The desalted pooled peptides were fractionated using an Agilent 1260 bioinert HPLC (Agilent, Santa Clara, CA, USA) equipped with an analytical column (4.6 mm × 250 mm, 5 μm particle) as described previously [24, 27]. High-pH peptide fractionation was performed with a 50 min gradient of 5-35% Solvent B at a flow rate of 0.2 mL/min using Solvent A (15 mm ammonium hydroxide) and Solvent B (15 mm ammonium hydroxide in 90% ACN). Totally, 96 fractions were collected every minute from 1 to 50 min. Subsequently, 96 fractions were non-contiguously pooled into 24 fractions. From each pooled fraction, we collected 5% of the fraction into an HPLC vial for global proteome analysis by LC-MS/MS [23]. For enrichment of phosphopeptide, the remaining 95% of each fraction were combined into 12 fractions.

Phosphopeptide Enrichment Using TiO2

Phosphopeptide enrichment was carried out as described in Humphrey SJ, et al. 2018 [28] with some modifications. Briefly, dried peptide fractions were resuspended using loading buffer composed of 6% (v/v) TFA and 80% ACN. TiO2 beads (Titansphere, GL Sciences Inc., Tokyo, Japan) were subsequently added to the peptides at a ratio of 10:1 beads/protein and incubated in a thermomixer at 2000 rpm for 30 min at 40℃. After centrifugation for 1 min at 3500 × g, the supernatant (containing non-phosphopeptides) was aspirated and discarded. Beads were suspended in the wash buffer (60% ACN and 1%

20
`

TFA). Washes were performed by a centrifugation four times with 1 mL of the wash buffer. Beads that were suspended in 100 μL of the transfer buffer (60% ACN and 0.1% TFA) were transferred to the top of a C8 StageTip, and centrifuged for 3-5 min at 3000 rpm. Phosphopeptides were eluted two times with 30 μL of the elution buffer (40% ACN and 15% ammonia solution) and collected by centrifugation into clean PCR tubes. Eluents were dried in a SpeedVac and acidified by the addition of 10% TFA. Phosphopeptides were desalted by loading onto a C18-SDB-RPS stageTip as described previously [29]. StageTips were washed with 0.2% TFA, and phosphopeptides were eluted with 60 μL of elution buffer (80% ACN and 5% NH4OH). Samples were immediately concentrated in a SpeedVac for 30 min at 45℃. Desalted peptides were resuspended in LC injection buffer (2% ACN and 0.1% formic acid) for LC-MS/MS analysis.

Mass Spectrometric Analysis and Database Search

Peptide samples were analyzed using a Q-Exactive plus mass spectrometer (Thermo Fisher Scientific, Bremen, Germany) coupled with an Easy-nLC system (Thermo Fisher Scientific, Odense, Denmark) as described previously [27]. Peptides were resuspended in 2% ACN and 0.1% formic acid and separated on a two-column system with a trap column and an analytical column (EASY-Spray column, 2 m particle size, 100 Å pore size, 75 μm id × 50 cm length, Thermo Fisher Scientific). Peptides were separated with a linear gradient of 8-32% solvent B (80% ACN and 0.1% formic acid) over 180 min at a flow rate of 300 nL/min. Spray voltage was set to 2.1 kV. Full MS was acquired with a mass range of 350-1800 m/z at a resolution of 70,000 at

`

m/z 200. MS2 scans were acquired at a resolution of 35,000. The top 15 precursor mass were selected in a data dependent acquisition (DDA) mode for MS/MS fragmentation by higher−energy collisional dissociation (HCD) at 32% normalized collision energy (NCE). The dynamic exclusion duration was set at 40 s and the isolation width was 0.7 Th with no offset. The resulting MS/MS spectra were searched against the UNIPROT human protein database (Uniprot release 2014_12, 88, 657 entries) with the SEQUEST−HT algorithm in Proteome Discoverer 2.2 (Thermo Fisher Scientific, Bremen, Germany). A maximum of two missed cleavage sites was allowed. Mass tolerances for precursor ions and fragment ions were set to 20 ppm and 0.02 Da, respectively. Carbamidomethylation of cysteine residues (+57.021 Da) and TMT tags on lysine residues and peptide N−termini (+229.163 Da) were set as fixed modification. Oxidation of methionine residues (+15.995 Da) and phosphorylation of serine, threonine, and tyrosine residues (+79.966 Da) were set as variable modifications. The false discovery rate (FDR) was determined using the percolator node. The FDR was set to 0.01 at the peptide spectral match (PSM), peptide, and protein levels. Only the PSMs that contained all ten reporter ions were considered for quantification. Proteins were quantified by summing reporter ion intensities across all matching PSMs. Normalization was performed based on the total reporter ion intensity in each channel. The mass spectrometry proteomics data have been deposited to the ProteomeXchange Consortium via the PRIDE [30] partner repository with the dataset identifier PXD018257 (proteome) and PXD018260 (phosphoproteome).

Bioinformatics Analysis

`

Statistical analysis for proteomic data was performed using the Perseus software [31]. Student's t test was employed for the proteome data set to identify statistically significant (permutation-based FDR at 5%) differences in expression at the protein levels, and for the phosphoproteome data set to identify statistically significant ($p < 0.05$) differences at the phosphorylation levels. For the hierarchical clustering analysis, multiple sample tests using one-way ANOVA was conducted ($p < 0.05$). Gene ontology (GO) annotation and pathway enrichment analysis were implemented with ClueGO plugin [32] of Cytoscape tool. Protein quantification data were also analyzed using gene set enrichment analysis (GSEA), and shown with density plots depicting the abundance of a gene set relative to the entire dataset (https://www.gsea-msigdb.org/gsea/msigdb/collections.jsp). Protein interaction network analyses of the significantly altered proteome and phosphoproteome in RPE data sets were performed with Cytoscape (v3.7.1) [33] software using the STRING database [34].

Cell Treatments

Confluent ARPE-19 monolayer cells maintained in 24-well plates were incubated with 10 mM L(+)-Lactic acid (Sigma), in the presence or absence of 3 mM monocarboxylate transporter blocker α-CHC (Sigma) for the designated time periods. HUVECs were seeded in 24-well plates at a density of 1×10^5/well. When the cells reached 60% to 70% confluence, cells were exposed to 10 mM L(+)-lactic acid with or without 3 mM α-CHC. THP-1 cells plated in 24-well plates at a density of 3×10^5/well and differentiated

`

into the macrophages by PMA treatment were incubated with 20 mM L(+)-Lactic acid with or without 3 mM α-CHC.

Animals

Female wild-type C57BL/6J mice (Samtako Co., Gyeonggi, Korea) between 7 and 8 weeks of age were used in this study. The study protocol was approved by the Seoul National University Animal Care and Use Committee (Approval No. SNU-160114-1). All animal experiments were conducted in accordance with the guidelines of the ARVO Statement for the Use of Animals in Ophthalmic and Vision Research.

Metabolite Extraction

RPE-choroid tissues were isolated from mice and metabolite extraction was performed according to a previously described method with minor modifications [35]. Briefly, freshly isolated tissues were homogenized in 100 μL 1 M perchloric acid (PCA) solution and incubated on ice for 30 minutes. After centrifugation at 15,871 $\times$ g for 15 minutes, 2 M KOH (0.25 μL per 1 μL PCA) was added to the supernatant to neutralize the PCA. After centrifugation at 15,871 $\times$ g for 15 minutes again, the resulting supernatant was subsequently used for lactate measurement.

Lactate Measurement

Lactate concentration was measured using a Lactate Colorimetric/Fluorometric Assay Kit (BioVision, Milpitas, CA, USA) according to the manufacturer's protocol.

`

ECAR and OCR Measurements

The ECAR (in mpH/min) and OCR (in pmol/min) were measured using the Seahorse XF-24 metabolic extracellular flux analyzer (Seahorse Bioscience, Billerica, MA, USA). ARPE-19 cells were seeded at a density of 5×10^4 cells per well in Seahorse cell plates and differentiated for 7 days. On the day of analysis, cells were washed two times with glucose free assay media (Seahorse Bioscience), and the ECAR and OCR in response to different concentrations (25, 50, and 100 μg/mL) of LPS were assessed in glucose-containing assay media. Experiments with the Seahorse system were performed according to the assay protocol consisted of repeated cycles of 2 min mixture; 2 min wait; and 4-5 min measurement. The ECAR and OCR were recorded and then calculated.

Cell Viability Assay

ARPE-19 cells were seeded 100 μL in a 96-well plate at a density of 2.5×10^4 cells per well, and maintained in DMEM/F12 media with reduced serum (1% FBS) for 7 days. The culture medium was changes every 2 days. The cells were stimulated with various concentrations of LPS for 24 h, and maintained in a humidified incubator at 37℃ in 5% CO_2. On the day of analysis, 10 μL of 5 mg/mL 3-(4,5-Dimethylthiazol-2-yl)-2,5-diphenyltetrazolium bromide (MTT, Sigma) was added to each well and incubated for an additional 4 h. After being centrifuged at 2400 rpm for 5 min, the supernatant was aspirated carefully. Then, 100 μL dimethylsulfoxide (DMSO) was added to each well and incubated for 20 min to dissolve the formazan crystals. The absorbance

`

was recorded at 560 nm with a microculture plate reader (Becton-Dickinson Labware, Lincoln Park, NJ, USA).

RNA Isolation and Real-Time RT-PCR

Total RNA was extracted from cells with Trizol (Invitrogen, Carlsbad, CA, USA) following the manufacturer's instructions. RNA concentration/quality was assessed by NanoDrop spectrophotometer (NanoDrop Technology, Wilmington, DE, USA). Equal amounts of RNA were reverse transcribed into cDNA with Reverse Transcription kits (Enzynomics, Daejeon, Korea) and gene expression was determined by quantitative real-time PCR using SYBR Green PCR Master Mix (Applied Biosystems, Foster City, CA, USA) on an ABI PRISM 7900 (Applied Biosystems). The relative mRNA expressions of each sample were normalized by β-actin and RPL37A and Student's unpaired t-test was used for statistical analysis. Sequences of primers used for amplifications were as follows: β-actin: FP, 5'-ATTGCCGACAGGATGCAGAA-3'; RP, 5'-GCTGATCCACATCTGCTGGAA-3'. RPL37A: FP, 5'-ATTGAAATCAGCCAGCACGC-3'; RP, 5'-AGGAACCACAGTGCCAGATCC-3'. VEGFA: FP, 5'-ATTGAAATCAGCCAGCACGC-3'; RP, 5'-AGGAACCACAGTGCCAGATCC-3'.

Laser-Induced CNV in Mice

Female C57BL/6J mice, aged 7 to 8 weeks, were anesthetized with an intraperitoneal injection of ketamine-xylazine (10 mg/kg), and the pupils were dilated with 1% tropicamide (Alcon Laboratories Inc., Fort Worth, TX, USA). Treatment with 831-nm 106 diode laser photocoagulation (75 μm spot size, 0.1-second duration, 120 mW) was delivered to each 3, 6, 9, and 12 o'clock

`

position of two disc-diameters from the optic disc by using an indirect head set delivery system of a photocoagulator (OcuLight; Iridex, Mountain View, CA, USA) and a handheld +78-diopter lens. The bubbling or pop sensing with laser photocoagulation was considered to be successful rupture of Bruch's membrane. These cases of successful rupture were included in this study. To evaluate the anti-angiogenic effect of blocking lactate uptake in macrophages, we injected 2 μL 3 mM α-CHC dissolved in PBS intravitreally 1 day after laser coagulation, when macrophages begin to infiltrate the burned area.

ELISA

ARPE-19 cells were treated with LPS for 24 h. The media was collected, centrifuged at 2500 rpm for 5 min to remove particulates, and stored at $-80℃$ until ELISA was performed. The protein concentration of the cells in each well was measured using bicinchoninic acid (BCA) protein assay kit (Thermo, Waltham, MA, USA) for the normalization of downstream cytokine quantification. Cytokine production from LPS-treated ARPE-19 cells was measured using the Duoset ELISA kit (R&D System, Minneapolis, MN, USA) according to the manufacturer's instructions.

Cells were treated with lactic acid for 24 hours. The media was collected, centrifuged at 587 $\times$ g for 5 minutes to remove particulates and stored at $-80℃$ until ELISA was performed.

Retina and RPE-choroid tissues were isolated from naive or CNV (3 days after laser) mice, and homogenized in ice-cold RIPA lysis buffer (Thermo Scientific) containing 1% protease inhibitor cocktail and 1% phosphatase cocktail (GenDepot). After centrifugation at 15,871 $\times$ g for 15 minutes, the

`

supernatant was used for ELISA assay. The secretion of VEGF was measured by use of the ELISA Duoset system (R&D Systems) according to the manufacturer's instructions.

Western Blotting

The cells were harvested with the 1X sample buffer (Biosesang, Seongnam, GG, Korea) containing a protease inhibitor and phosphatase inhibitor cocktail (GenDepot). Then, the total cell lysates were sonicated for 30 s and heated to 100℃ for 10 min. The proteins were separated on 8% polyacrylamide gels followed by transfer onto polyvinylidene difluoride (PVDF) membranes (Merck Millipore, Burlington, MA, USA). ICAM-1 (Santa Cruz Biotechnology Inc.), HMOX-1 (Santa Cruz Biotechnology Inc.), phosphor-β-catenin (Ser552; Cell Signaling Technology, Danvers, MA, USA), β-catenin (Santa Cruz Biotechnology Inc.), and β-actin (Santa Cruz Biotechnology Inc.) were used at 1/2000 dilutions.

Immunohistochemistry

THP-1 cells differentiated with 15 ng/mL of PMA for 48 hours were treated with lactic acid for 18 hours, and fixed for 15 minutes in 4% paraformaldehyde. After blocked in 5% FBS in PBS containing 0.3% Triton X-100 for 1 hour, cells were incubated at 4℃ overnight with the following primary antibodies: FITC-conjugated CD68 (KP1; Santa Cruz Biotechnology, Inc.) and APC-conjugated anti-mouse VEGF (C-1, Santa Cruz Biotechnology, Inc.). The cells were rinsed and washed three times with PBS. Finally, to stain nuclei, cells were treated for 15 minutes with 3 μM of the nuclear stain 4',6-

`

diamidino-2-phenylindole (DAPI). The stained cells were observed under a Olympus FV1000 Confocal Scanning Scope. The VEGF intensity was measured using ImageJ software (http://imagej.nih.gov/ij/; provided in the public domain by the National Institutes of Health, Bethesda, MD, USA).

Three days after laser photocoagulation, eyes were enucleated from mice and fixed for 1 hour in 4% paraformaldehyde. After removal of the retina, RPE-choroid tissues were incubated with rat anti-mouse F4/80 (Bio-Rad, Richmond, CA, USA) and APC-conjugated anti-mouse VEGF (C-1; Santa Cruz Biotechnology, Inc.) at 48℃ overnight. The flat-mount was washed with PBS 10 times for 10 min on an orbital shaker at room temperature and then incubated with Alexa-Fluor 488-labeled goat anti-rat IgG (Molecular Probes) for 1 h on an orbital shaker at room temperature. The stained tissues were examined under an Olympus FV1000 Confocal Scanning Scope. The areas of infiltrated macrophage and secreted VEGF were measured using ImageJ software. Histology Fixed globes after laser induction were embedded in paraffin and processed for standard hematoxylin and eosin (H&E) staining to assess standard morphology. Stained sections were digitized using a light microscopy (Labophot; Nikon, Tokyo, Japan).

CNV Quantification

For the assessment of CNV, RPE-choroid tissues isolated from the eyes 7 days after laser were stained with Alexa-Fluor 594-conjugated isolectin B4 (Molecular Probes) to visualize CNV. Images acquired with Olympus FV1000 Confocal Scanning Scope were processed in IMARIS imaging software (Bitplane, Zurich, Switzerland) to quantify IB4-positive CNV volume.

29
`

Flow Cytometry

THP-1 cells differentiated with 15 ng/mL of PMA for 48 hours were treated with lactic acid for 18 hours. After fixed and permeabilized, cells were stained with APC-conjugated anti-mouse VEGF (C-1; Santa Cruz Biotechnology, Inc.). Labeled cells were analyzed using LSR-II cytometer (BD Biosciences, San Jose, CA, USA), and the data were analyzed using FlowJo Software (version 7.6.2; Ashland, OR, USA).

Laser-treated eyes were enucleated microsurgically 1, 3, 7, 14, and 21 days after laser treatment. After removing the anterior segment and vitreous humor, the posterior segment containing the retina and RPE-choroid was subsequently dissociated enzymatically for 1 hour with 1 mg/mL type I collagenase (Sigma) in the presence of 50 units/mL DNase I (Sigma). Single-cell suspension in PBS was washed by centrifugation at 685 × g for 5 minutes, and then cell pellets were suspended with 200 μL FACS buffer containing 1% BSA and 0.1% sodium azide. For surface staining, the following antibodies were used: Q655-conjugated anti-mouse CD45 (clone: 30-F11; eBioscience, San Diego, CA, USA), PE-conjugated anti-mouse F4/80 (clone: BM8; eBioscience), APC eFluor 780-conjugated anti-mouse CD11b (clone: M1/70; eBioscience), V450-conjugated anti-mouse Gr-1 (clone: RB6-8C5; eBioscience), FITC-conjugated anti-rat CD206 (clone: MR5D3; AbD Serotec, Raleigh, NC, USA). To detect intracellular cytokines, cells were fixed and permeabilized in BD Perm/Wash buffer (BD Pharmingen, San Diego, CA, USA) before incubation with the following antibodies: APC-conjugated anti-mouse VEGF (C-1, Santa Cruz Biotechnology, Inc.). Labeled cells were analyzed

`

using LSR-II cytometer (BD Biosciences), and the data were analyzed using FlowJo Software (version 7.6.2).

Tube Formation Assay

Growth factor-reduced Matrigel (Corning) was thawed at 4℃ overnight. Each well of a prechilled 24-well plate was coated with 100 μL Matrigel and incubated at 37℃ for 40 minutes. HUVECs (3×10^4 cells) were suspended in 100 μL EGM-2 media and seeded with 400 μL macrophage conditioned media. After 12 hours of incubation at 37℃ with 5% CO_2, endothelial cell tube formation was visualized with Calcein AM (Corning) and then imaged using a Leica CTR6000 fluorescence microscope (Wetzlar, Germany). The number of capillary-like structures was quantified by manual counting of low-power fields (×10). Five independent fields were assessed for each well, and the average number of branches per field (magnification, ×10) was determined.

Statistical Analysis

All results are expressed as the means $\pm$ SEM and visualized using Prism version 6 (Graphpad Software, La Jolla, CA, USA). The student's unpaired t test (two-tailed) was used to calculate statistical significance between experimental groups. $p < 0.05$ was defined to be statistically significant.

`

6.3. RESULTS

Induction of Inflammation on ARPE-19 Monolayer for Proteomic Analysis

For proteomic analysis to understand the molecular mechanisms causing pathological progression in RPE, polarized monolayer culture of ARPE-19 cells was performed. The expressions of junctional protein ZO-1, visual cycle protein RPE65, and polarity protein $Na^+K^+ATPase$ were identified using immunofluorescence staining (Figure 1A). To determine the concentration of LPS that could elicit both metabolic and pro-inflammatory responses in RPE, extracellular acidification rate (ECAR)/oxygen consumption rate (OCR) and inflammatory cytokine levels were assessed with different concentrations of LPS. I observed that 50 μg/mL of LPS significantly increased the ECAR and OCR after treatment and facilitated the secretion of inflammatory cytokines IL-6, TNFα, and IL-12 in ARPE-19 cells, with no morphological changes but an apparent decrease in cell viability, indicating inflammation-driven pathological progression had begun within 24 h (Figures 1B-E). In addition, ARPE-19 cells showed significant metabolic changes between 30 min and 1 h after LPS treatment, implying that important signaling cascades has been initiated between these two time points. Therefore, I decided to investigate proteome and phosphoproteome changes in 50 μg/mL LPS-treated ARPE-19 cells to verify inflammation-driven pathology at the following time points; at 45 min for early signal transduction events and at 24 h for late proteome changes. The 10-plex TMT isobaric labeling quantitative proteomic method with high pH reversed phase (high pH-RP) chromatography was used to identify alterations in both abundance and phosphorylation status in protein

`

extracts (Figure 1F). The data obtained from comparative MS analysis were processed with various bioinformatics tools.

Quantitative Proteomic and Phosphoproteomic Analyses of ARPE-19 Cells

The reproducibility of proteome results obtained from three biological replicates of each group was evaluated by comparing the relative protein quantification. Multi-scatter plots with Pearson's correlation coefficients between approximately 0.991 and 0.999 demonstrated strong reproducibility between biological replicates in each experimental group (Figure 2). The principle component analysis (PCA) of the data set from both the ARPE-19 proteome and phosphoproteome also showed good clustering of the biological replicates, as well as clear separation between LPS-treated and untreated control (0 min; Figure 3A). Using a false discovery rate (FDR) of 1%, I identified 130,878 unique peptides from 8984 proteins with average sequence coverage of 31% (Figure 3B). Among the differentially expressed proteins (DEPs), a subset of 261 proteins showed more than a 1.5-fold change in abundance after LPS challenge (adjusted $p < 0.05$). For data sets of phosphopeptides, after internal normalization based on total amounts, they were further normalized to the corresponding protein abundance for each phosphopeptides. Analysis to examine the difference of phosphorylation status between control and LPS-treated ARPE-19 cells led to the identification of 20,632 unique phosphopeptides from 3207 phosphoproteins with 3103 phosphorylation sites (Figure 3C). Among these, 618 phosphopeptides corresponding to 466 proteins, and 2774 phosphopeptides corresponding to 1358 proteins were differentially regulated after LPS challenge for 45 min and

33
`

24 h, respectively (p < 0.05). In comparison of proteomic and phosphoproteomic data, we found that 2561 proteins overlapped between proteins and phosphoproteins (Figure 3D). Frequency distributions showed that most phosphoproteins were not significantly affected by LPS stimulus at either early or late time points as the average log2-fold changes centered around zero (Figure 3E). Distribution patterns of statistical significance (−log p values) and magnitude of change (log2 fold change) for all proteins and phosphoproteins identified at each time point were visualized using volcano plots (Figure 3F).

Functional Annotation of the Identified Proteins

To investigate biological processes associated with inflammation-driven pathology, I performed a hierarchical clustering (HCL) analysis and gene ontology (GO) enrichment analyses. HCL analysis revealed two separate groups comprising of up- and down-regulated proteins, as compared to the untreated control (Figure 4A). The DEPs in each time point were annotated and functionally classified using the ClueGO plugin of the Cytoscape tool that can decipher GO and pathway annotation networks with a hypergeometric test and study functional correlations among pathways by the kappa coefficient calculation [36]. In contrast to the DEPs at 45 min, where few significant changes (q < 0.05) were observed except for KIAA1522, the 4192 DEPs at 24 h were grouped into multiple pathways. GO analysis of the identified proteins showed strong downregulation of proteins related to mitochondrial metabolism and the cell cycle checkpoint. In contrast, perturbations in lipid

`

and amino acid metabolism, and overall upregulation in cell-matrix adhesion, endoplasmic reticulum (ER) stress, and extrinsic apoptotic signaling were observed after LPS challenge (Figure 4A). The 261 proteins that showed more than a 1.5-fold change in abundance in response to LPS challenge also grouped multiple pathways including response to reactive oxygen species and DNA damage response. To obtain functional protein profiles associated with the differential expression patterns, I also conducted gene set enrichment analysis (GSEA) by ranking gene products according to a differentiability statistic (e.g., ratio of expression in LPS-treated versus control) using GSEA's Molecular Signature Database (https://www.gsea-msigdb.org/gsea/msigdb/collections.jsp; Figure 4B). Interestingly, with significant metabolic perturbations, two important pathways regulated by the 153 up- and downregulated proteins in our study were essential for leukocyte homeostasis and the cell-matrix adhesion. In particular, the high-mobility group box 1 (HMGB1) and hypoxia-inducible factor 1α (HIF1α), known as pro-angiogenic and pro-inflammatory factors in RPE, showed increased abundance during inflammation in the RPE. Intracellular adhesion molecule 1 (ICAM-1), fibronectin-1 (FN1), fibrillin-1 (FBN1), and thrombosponin-1 (THBS1), all associated with cellular adhesion and especially known to be increased in high-risk RPE, were also upregulated. In addition to the strong downregulation of matrix metallopeptidase 14 (MMP14), a critical enzyme for maintaining the physiological balance between synthesis and disintegration of structural elements of Bruch's membrane (BrM), junctional adhesion molecule 3 (JAM3), which regulates the recruitment of N-cadherin and ZO-1 to tight junction formation, was also decreased by inflammation (Figure 4B).

`

Phosphoproteome Analysis

To further investigate the LPS-induced signal pathways governed by protein phosphorylation and dephosphorylation, I first performed HCL analysis using a phosphoproteome data set. Interestingly, clustering of the phosphoproteome revealed a clear segregation into three clusters, reflecting three distinct patterns of phosphorylation progression by LPS challenging (Figure 5A). Differentially phosphorylated peptides (DPPs) of cluster 1 (449 of 2376, 18.90%), which exhibited increased phosphorylation at 24 h post-challenge, were selectively enriched for several GO terms, including cholesterol metabolic process, cell aging, cell-matrix adhesion, and cell death. DPPs of cluster 2 (1742 of 2376, 73.32%), which exhibited dephosphorylation at 24 h post-challenge, were enriched for GO terms including protein kinase activity, cellular response to DNA damage, and response to cytokine. Finally, DPPs of cluster 3 (185 of 2376, 7.79%) that exhibited phosphorylation at 45 min after LPS challenge were enriched for GO terms including the p38 MAPK cascade and β-catenin-TCF complex assembly (Figure 5A). For detailed identification of early phosphorylation events after LPS challenge, I reperformed HCL analysis using phosphoproteome data sets of 0 min and 45 min (Figure 6A). Among the two distinct clusters, DPPs of cluster 1 (196 of 618, 31.88%) that exhibited phosphorylation at 45 min after LPS challenge were also enriched for I-κB phosphorylation and cell death, whereas cluster 2 (422 of 618, 68.45%) was enriched for GO terms including ER stress and regulation of DNA repair. The significantly altered phosphorylation status of key protein components after stimulation with LPS for 45 min and 24 h was visualized using a heatmap with identified phosphosites (Figure 5B).

36

`

Interestingly, protein kinase C delta (PRKCD) involved in NF$-\kappa$B activation was phosphorylated at residue Ser$-$304 (100%). In addition, $\beta$$-$catenin (CTNNB1), involved in the regulation of inflammation via crosstalk with NF$-\kappa$B, was phosphorylated at residue Ser$-$552 (99.8%) after LPS challenge for 24 h, whereas occludin (OCLN), whose phosphorylation has been known to occur in the maintenance of tight junction integrity, was identified to be significantly dephosphorylated at residue Ser$-$321 (100%). The significantly altered phosphorylation status of key protein components by stimulation with LPS for 45 min was also identified with phosphosites in Figure 6B.

Protein Interaction Network of LPS$-$Treated ARPE$-$19 Cells

To examine the relationship between the significantly altered proteome and phosphoproteome, I constructed a protein$-$protein interaction (PPI) network using Cytoscape software. The separated analysis of the proteomics and phosphoproteomics datasets were depicted in one$-$dimensional views of cellular processes by integrating the information regarding protein abundances, activation status, and molecular interactions, with the goal of determining their complex interplay during inflammation$-$driven pathogenesis. In this network modeling, I focused on the 106 DEPs and 30 DPPs that were selected based on the GSEA and ClueGO database (Figure 4B, Figure 5B, Figure 6B). As shown in Figure 7, a total of 136 nodes were largely interconnected with 1094 edges, suggesting they are multifunctional and interdependent. These nodes were grouped and represented by 16 GO$-$biological process terms that were closely associated with RPE pathobiology.

`

Finally, to validate our MS-based quantification of protein and phosphoprotein, I performed Western blot analysis for the two proteins (ICAM-1 and heme oxygenase-1, HMOX-1) and one phosphoprotein (β-catenin) that were involved in distinct pathways. Consistent with the proteome data, ICAM-1 was shown to be upregulated, while HMOX-1 was downregulated after LPS treatment for 24 h (Figure 8A). The phosphorylation of β-catenin at Ser-552 residue was also identified as increased by LPS challenge for 24 h (Figure 8B). These findings indicate that the TMT labeling-based proteomic and phosphoproteomic analysis performed in this study possesses sufficient analytical power to confidently reveal changes in protein and phosphoprotein levels relevant to inflammation-driven pathology.

Elevated Lactic Acid Levels in RPE-Choroidal Region of CNV

CNV was induced by laser burn and RPE-choroid tissue was isolated for metabolite extraction (Figure 9A). CNV lesions at day 1 were stained with H&E and found to have broken RPE layers and Bruch's membrane rupture compared with unlasered controls (Figures 9B, 9C). To evaluate the lactic acid concentration in CNV, metabolites extracted from RPE-choroid tissues were analyzed by ELISA. As shown in Figure 9D, lactic acid levels in RPE-choroid tissues were significantly increased compared with unlasered controls.

Lactic Acid Induces Macrophages to Become Pro-angiogenic

During CNV development, crosstalk of RPE with immune cells and the vascular system has been reported to be a key event in CNV development [17]. Increased production of VEGFA by cells participating in these processes has

`

been implicated as the main contributor to abnormal angiogenesis, and has therefore been a therapeutic target for neovascular AMD [11, 37]. Considering previous studies on the signal-inducing ability of lactic acid, we wondered whether lactic acid affects VEGF secretion by cell types in the eye. To directly study the contribution of lactic acid to the VEGF expression of RPE, endothelial cells, and infiltrated macrophages, we conducted in vitro cell line experiments using ARPE-19, HUVEC, and PMA-differentiated THP-1 macrophages. Cells were treated with 20 mM lactic acid. VEGFA mRNA and VEGFA protein expression were assessed by real-time RT-PCR and ELISA, respectively. Gene transcript and protein expression for VEGFA in ARPE-19 and HUVECs did not change after lactic acid treatment (Figures 10A, 10B); however, PMA-differentiated THP-1 macrophages showed significant increase in VEGFA mRNA expression and peaked at 12 hours post-stimulation by more than 3-fold (Figure 10C). Secreted VEGF also significantly increased by approximately five times in THP-1 macrophages incubated with lactic acid for 24 hours, which was reduced by pretreatment of 3 mM monocarboxylate transport blocker, α-CHC (Figure 10D). This was further confirmed by analyzing VEGF content of THP-1 macrophages after incubation with lactic acid for 18 hours using flow cytometry and immunofluorescence staining technique (Figure 11). Importantly, THP-1 macrophages exposed to media acidified to pH 4.5 with HCl did not show any significant changes in VEGF expression, indicating that VEGF upregulation by lactic acid is not due to the acidification of culture media.

Then, to identify whether lactic acid–stimulated macrophages promote angiogenesis, I performed HUVEC tube formation assay. PMA-differentiated

39

`

THP-1 macrophages were stimulated with 20 mM lactic acid for 12 hours, and media was then changed. Tube-forming ability of supernatant collected after 24-hour incubation was compared with that of nonstimulated cells and α-CHC–pretreated cells. As shown in Figure 12, enhanced endothelial tube formation was observed in lactic acid–conditioned media compared with that of non-treated media, whereas supernatant of α-CHC–pretreated lactic acid–stimulated macrophages exhibited clear reduction in the amount of tube formation of HUVECs. A 5-fold increase in number of branches formed by lactic acid–conditioned media was also substantially reduced by α-CHC and lactic acid co-treated conditioned media (Figure 12C), indicating that macrophages exposed to lactic acid are programmed to be pro-angiogenic.

Infiltration and VEGF Expression of Macrophages in CNV

To investigate the effect of lactic acid in vivo, I first assessed macrophage infiltration into CNV lesions by flow cytometric analysis. The number of recruited macrophages ($CD45^+CD11b^+Gr1^-F4/80^+$) increased at 1 day after laser and peaked at 3 days with an increase of more than 10-fold compared with that of nonlasered controls (Figures 13A, 13B). Intracellular VEGF content per single macrophage cell at day 3 after laser treatment was significantly upregulated compared with that of unlasered controls (Figures 13C, 13D), providing further evidence of the pro-angiogenic properties of macrophages.

Inhibitory Effect of α-CHC on Neovascularization

`

The effect of lactic acid on VEGF expression in macrophages and subsequent aberrant neovascularization was confirmed by intravitreal injection of monocarboxylate transporter (MCT) blocker α-CHC 1 day after CNV induction. Injection of 2 μL 3 mM α-CHC resulted in significant reduction of VEGFA contents in macrophages at 3 days after laser shot (Figures 14A, 14B). Flatmount immunofluorescence staining also showed the significant reduction of VEGF-positive area (383,738 $\pm$ 196,716 μm^2) within F4/80-stained macrophage area compared with controls (523,378 $\pm$ 165,071 μm^2) (Figures 14C, 14E), although the area of infiltrated macrophages showed no significant changes (Figure 14D). The VEGF levels in RPE-choroid tissues at day 3 (2120.5 $\pm$ 286.4 VEGF pg/tissue g) and isolectin B4 (IB4)-positive endothelial cells at day 7 (141,472.9 $\pm$ 49,186.4 μm^3) after laser burn were both substantially reduced by α-CHC injection (1138.9 $\pm$ 109.7 VEGF pg/tissue g and 74,160.6 $\pm$ 12,339.5 μm^3, respectively) (Figures 14F–H), suggesting that modulation of macrophages by blocking lactic acid transport has a promise for CNV therapeutics (Figure 15).
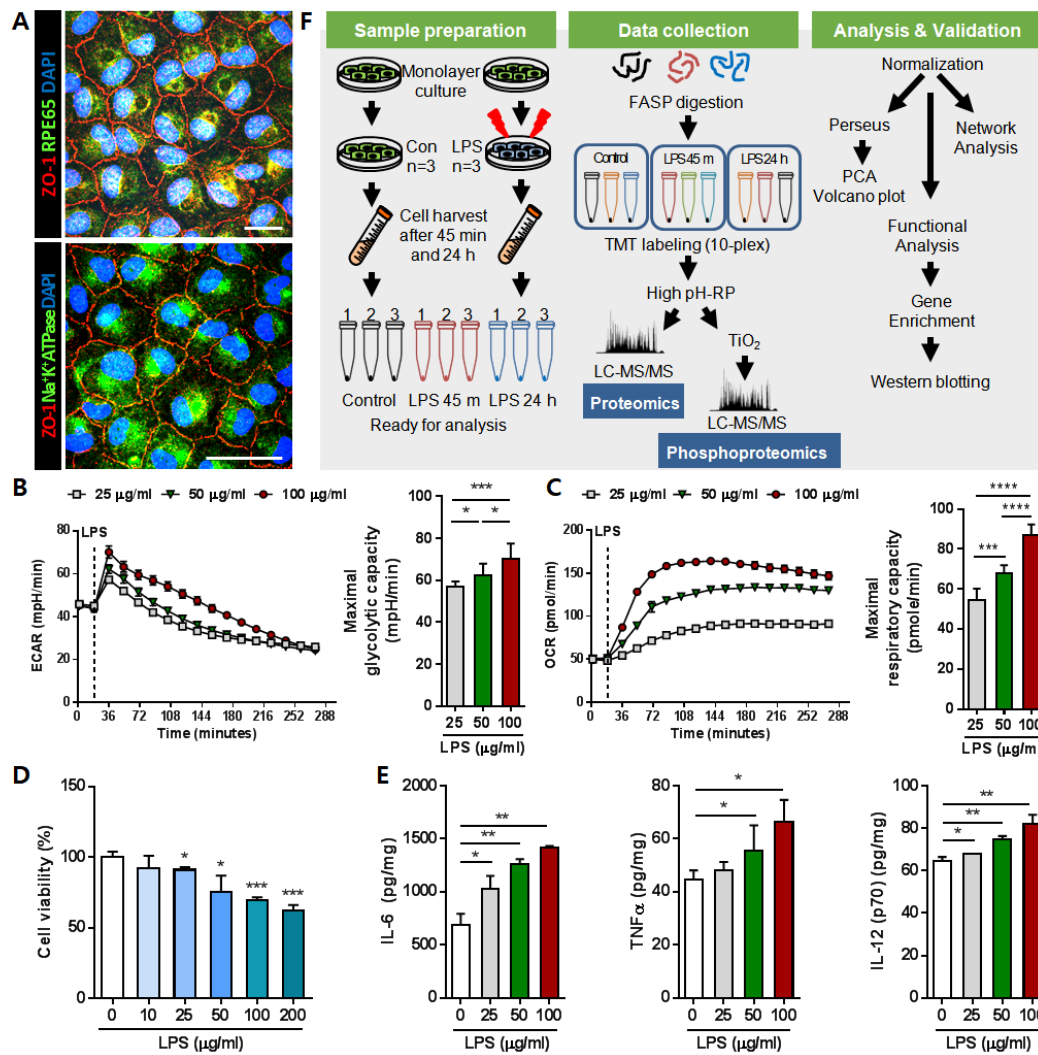
`

Figure 1. Experimental setup and workflow to investigate lipopolysaccharide (LPS)−stimulated ARPE−19 proteome and phosphoproteome. (A) Immunofluorescence images of polarized ARPE−19 cells stained for ZO−1 (red) and RPE65 (green) or Na⁺K⁺ATPase (green). Scale bar: 25 μm. (B, C) Real−time measurements of extracellular acidification rate (ECAR) and oxygen consumption rate (OCR) for assessing metabolic responses to different concentrations of LPS in ARPE−19 cells. (D) Cell viability measurement of ARPE−19 cells stimulated with different concentrations of LPS for 24 h. (E) Cytokine production of ARPE−19 cells treated with different concentrations of LPS for 24 h. Bars indicate means ± SEM. $*p <$

42

`

0.05, **p < 0.01, ***p < 0.001, ****p < 0.0001. (F) Pipeline for the tandem-mass tag (TMT)-based proteomic/phosphoproteomic approach to LPS-treated ARPE-19 cells.
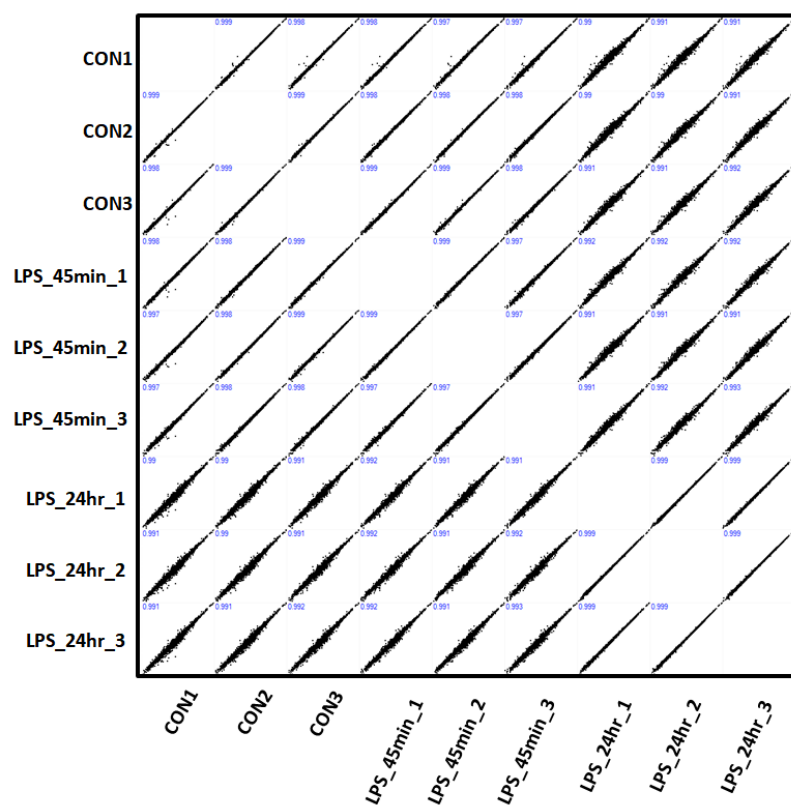
`

Figure 2. Reproducibility of global proteomic quantification. Multi-scatter plot of label-free protein intensities between different replicates of the samples was depicted with the Pearson correlation coefficient values.
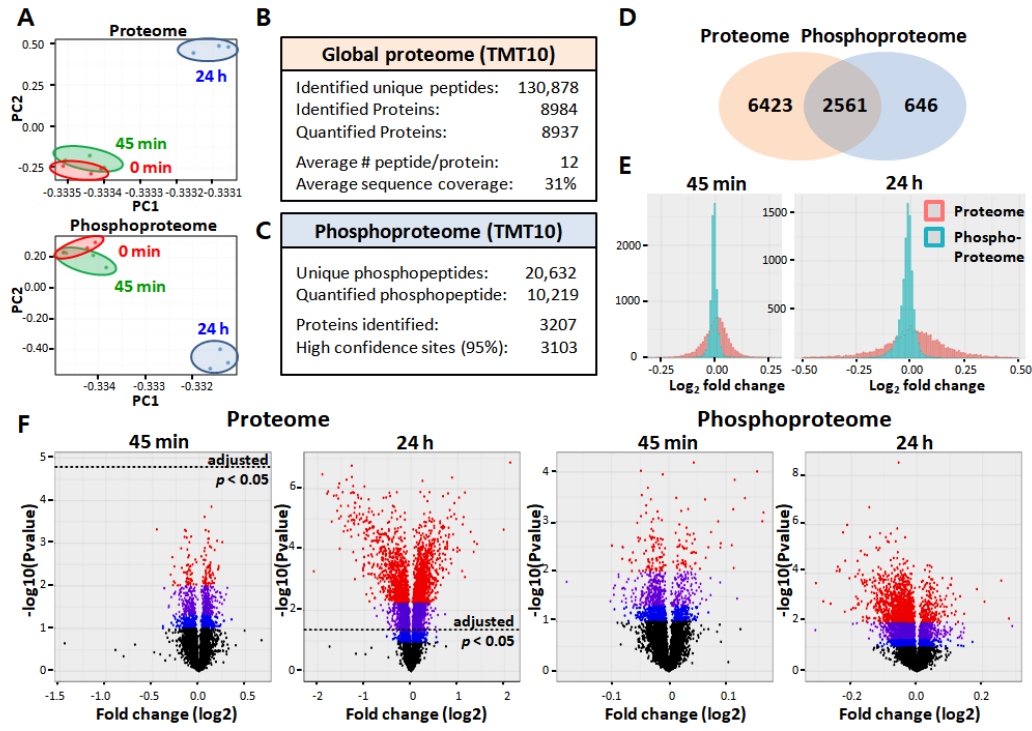
`

Figure 3. Overview of the LPS-stimulated ARPE-19 proteome and phosphoproteome. (A) Principal component analysis (PCA) of quantified proteins at total protein level and quantified phosphopeptides from three different treatment groups in triplicate. (B, C) Results of proteome/phosphoproteome experiments. (D) Venn diagram of the overlap of proteins identified in proteome profiling experiments with phosphoproteins identified in phosphoproteomic experiments. (E) Log fold-change distribution histogram comparing proteome (red) and phosphoproteome (blue) identified at two treatment time points. (F) Volcano plots from different group comparisons. Blue dots represent $p < 0.1$, $|\log2(\text{fold change})| > 0$, purple represent $p < 0.05$, $|\log2(\text{fold change})| > 0$, and red represent $p < 0.01$, $|\log2(\text{fold change})| > 0$. Black dotted line means p-value (adjusted) threshold of 0.05 to filter the statistically significant results.
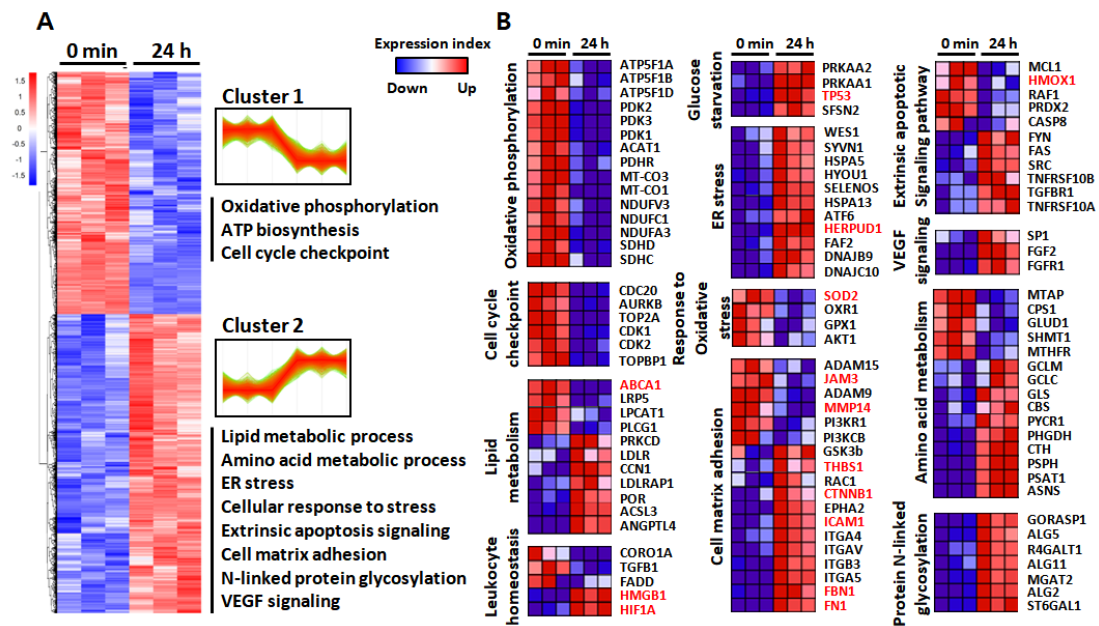
Figure 4. . Visualization of changing proteins and their biological pathways. (A) Hierarchical cluster (HCL) analysis of differentially expressed proteins upon 24 h treatment of 50 μg/ml LPS, according to their abundance profile with significantly enriched biological process gene ontology (GO) terms within clusters. (B) Heat maps of the most enriched proteins between groups that strongly contributed to pathway enrichment scores (ES) in gene set enrichment algorithm (GSEA). The unique proteins significantly altered by LPS treatment were marked in red.

`

Figure 5. HCL analysis of the identified phosphoproteins with differential phosphorylation intensities. (A) HCL analysis of significantly altered phosphosites upon treatment of 50 μg/mL LPS for 45 min and 24 h, according to their abundance profile, with significantly enriched biological process GO terms within clusters. (B) Heat map showing phosphorylation status of 41 phosphosites that were significantly changed among three time point measurements.
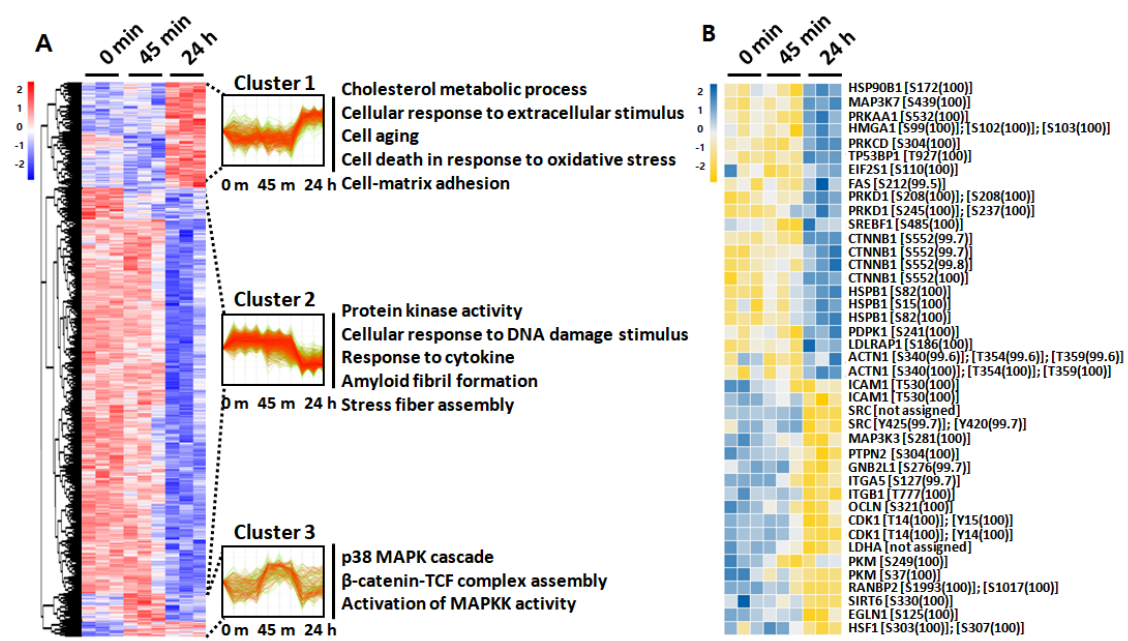
Figure 6. HCL analysis of the identified phosphoproteins with differential phosphosite intensities. (A) HCL analysis of significantly altered phosphosites upon 45 min treatment of 50 μg/ml LPS, according to their abundance profile with significantly enriched biological process GO terms within clusters. (B) Heat map showing phosphorylation status of 16 phosphosites that were significantly changed between two time point measurements.
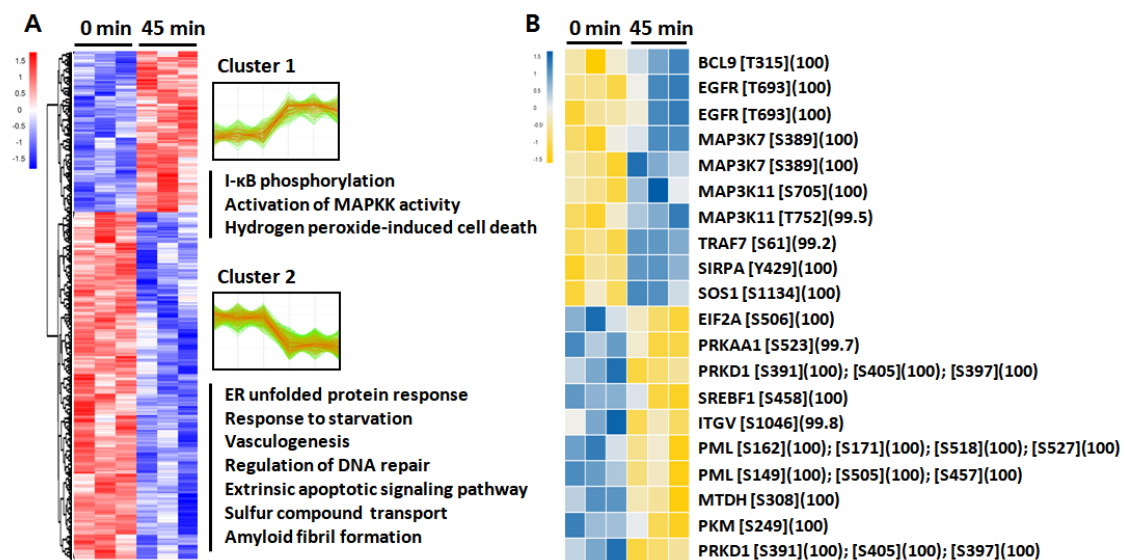
`
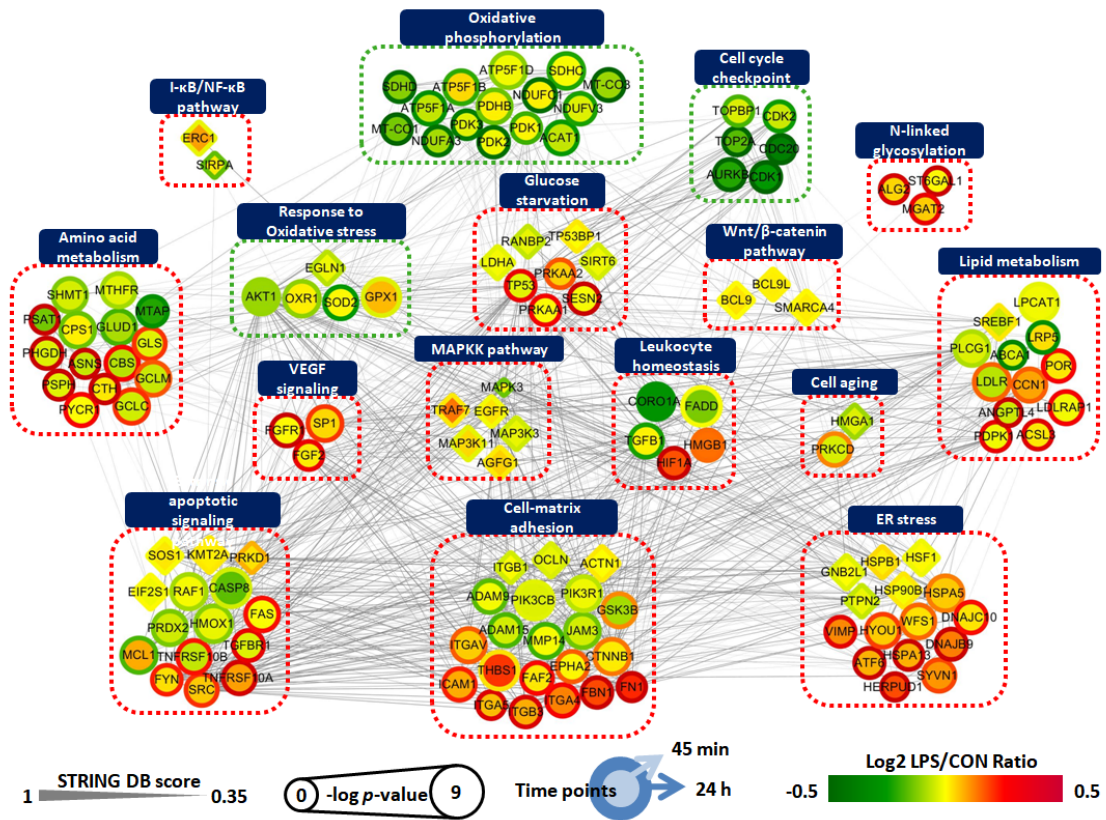
Figure 7. Network analysis of proteins related to inflammation−driven pathology of ARPE−19 cells. A total of 136 differentially expressed proteins and phosphoproteins involved in differentially regulated biological processes were grouped according to their function. Circle indicates DEP and diamond indicates DPP. Node colors represent an increase (red) and decrease (green) in LPS−treated ARPE−19 cells for 45 min (center) and 24 h (boundary) compared to untreated controls. The color bar represents the gradient of log2 protein ratios. The size of a node represents $\log10(p$−value). The edges represent PPIs obtained from the STRING database [34]. Pathways with red dotted lines indicate clusters upregulated by LPS and pathways with green dotted lines indicate clusters downregulated by LPS. All are indicated by gene symbol.

`
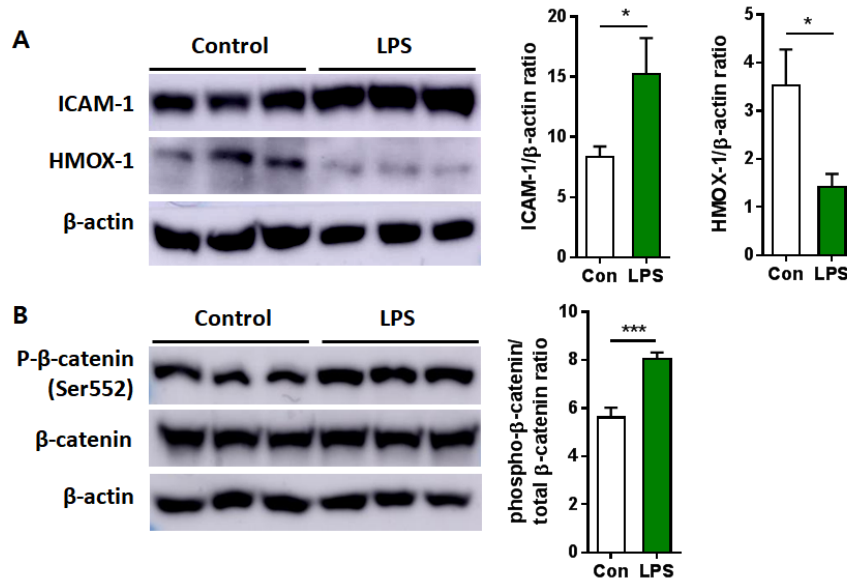
Figure 8. Western blot analysis of proteins and phosphoprotein included in the pathways related to inflammation−driven pathogenesis in ARPE−19 cells. ARPE−19 cells were challenged with 50 μg/ml LPS for 24 h. **(A)** Representative western blot protein bands and histograms for ICAM−1 and HMOX−1 normalized to β−actin. **(B)** Representative western blot protein bands and histograms of phospho−β−catenin (Ser552) normalized to total form. Bars indicate means $\pm$ SEM. $*p < 0.05$, $***p < 0.001$.

`
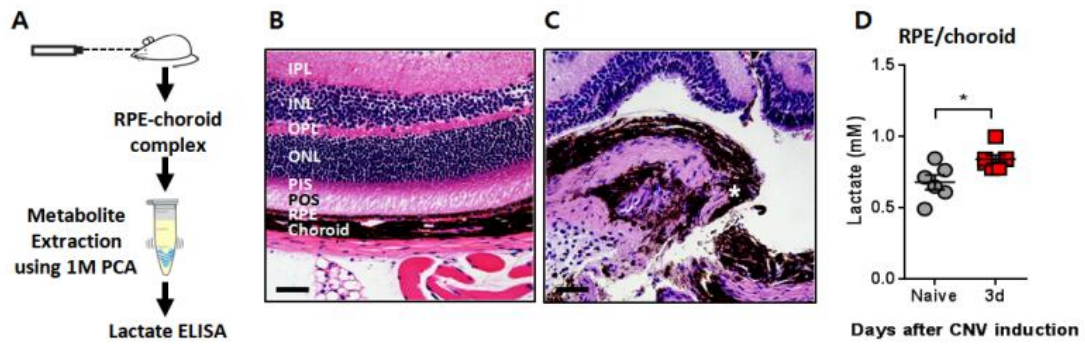
Figure 9. Lactic acid is increased in RPE−choroid regions of CNV−induced mice. (A) Schematic image describing CNV inducing and lactic acid measurement. (B, C) Representative retinal histology before injury (B) and 1 day after injury (C). H&E stained. n = 6. Broken RPE is marked by the asterisk. IPL, inner plexiform layer; INL, inner nuclear layer; OPL, outer plexiform layer; ONL, outer nuclear layer; PIS, photoreceptor inner segment; POS, photoreceptor outer segment. Scale bars: 50 lm. (D) Lactate concentrations of RPE−choroid regions measured by a lactate colormetric/fluorometric assay kit. n = 6. Bars indicate means ± SEM. *$p < 0.05$.

`
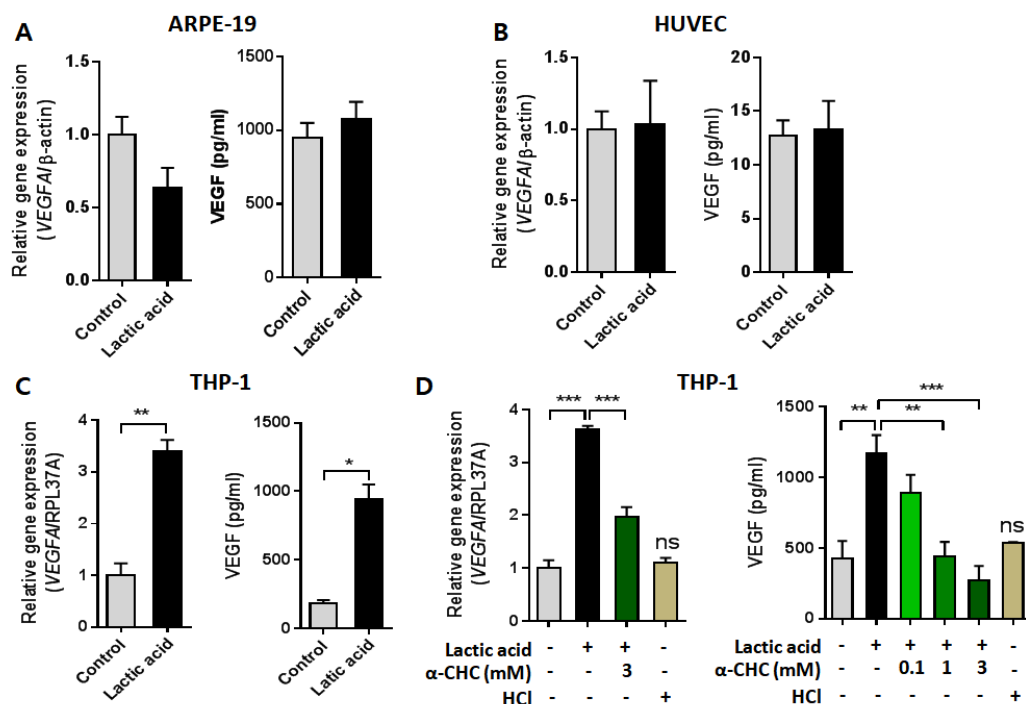
Figure 10. Lactic acid induces VEGF expression in macrophages. (A-C) Expression analysis by qPCR and ELISA of VEGF in ARPE-19 (A), HUVEC (B), and PMA-differentiated THP-1 macrophages (C) was conducted following incubation with control or 20 mM of lactic acid (LA)-treated medium. (D) Expression analysis of VEGF in THP-1 macrophages was conducted following incubation with lactic acid ± MCT blocker α-CHC and acidic pH necessary for the effect of lactic acid. Data are representative of three independent experiments. Bars indicate means ± SEM. $*p < 0.05$, $**p < 0.01$, $***p < 0.001$.
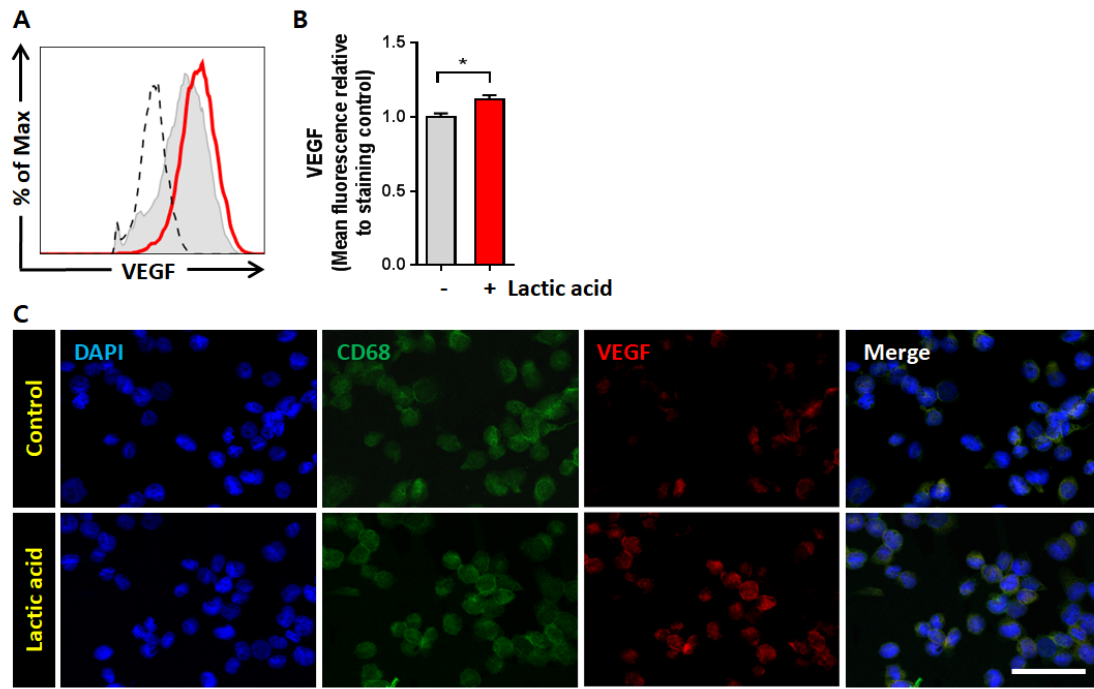
Figure 11. Lactic acid enhances VEGF expression in THP-1 macrophages. (A, B) FACS analysis of PMA-differentiated THP-1 macrophages following stimulation of 20 mM lactic acid for 18 h was conducted. Representative histogram (A) and MFI values (B) are shown (n=3 per group). Bars indicate means ± SEM. $*p < 0.05$ (C) Representative images of immunofluorescence staining of DAPI (blue), CD68 (green), and VEGF (red) in THP-1 macrophages following 20 mM lactic acid treatment are shown (n=3 per group). Scale bar = 50 μm.

`
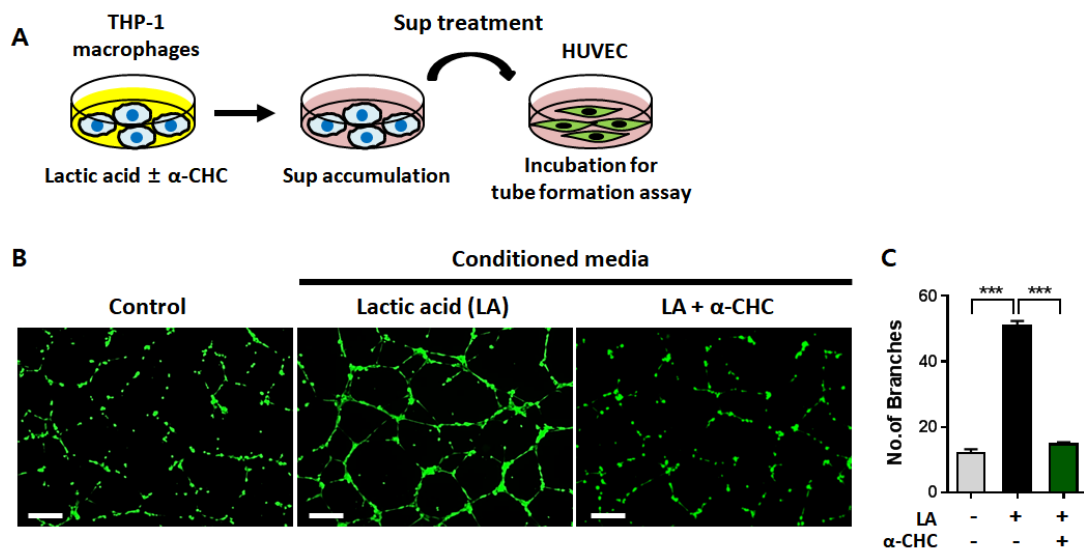
Figure 12. Lactic acid−stimulated THP−1 macrophages facilitate angiogenesis. (A) Schematic image describing tube formation assay. HUVECs were seeded onto Matrigel−coated plates with control THP−1 supernatant, lactic acid−stimulated THP−1 supernatant in the presence or absence of α−CHC. (B) Representative images of capillary−like structures stained with Calcein AM are shown. (C) Total branching points were calculated using ImageJ software. Data are representative of three independent experiments. Bars indicate means ± SEM. ***$p < 0.001$. Scale bar = 100 μm.

`
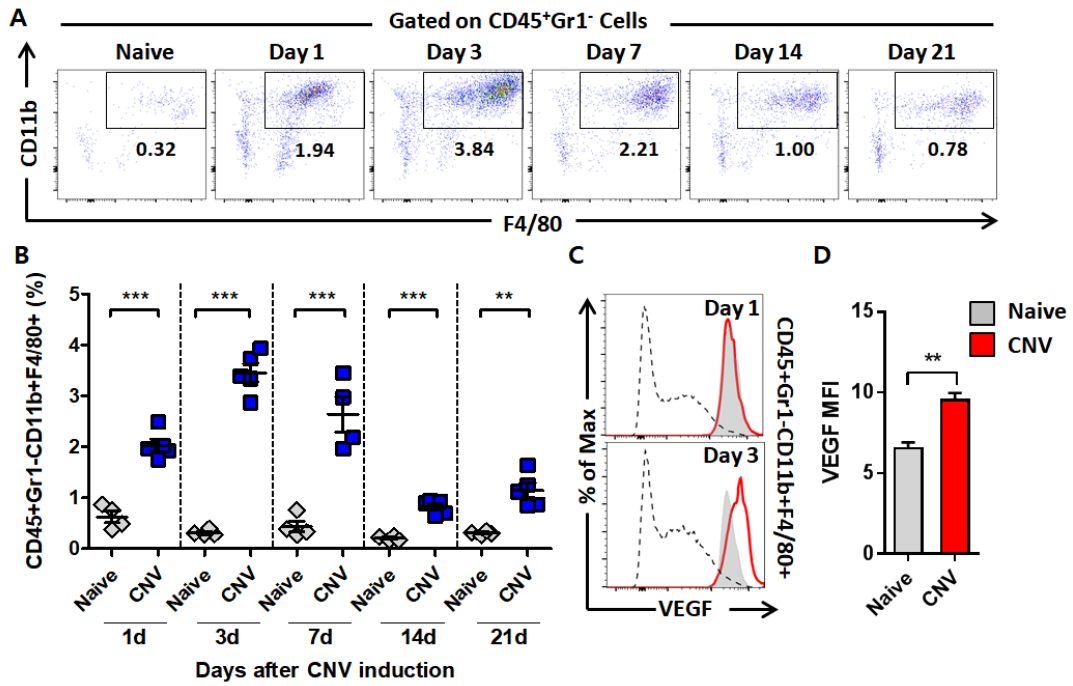
Figure 13. Macrophage infiltration and their VEGF secretion are increased in RPE−choroid regions in CNV mice. (A, B) Posterior eyecups of mice after induction of CNV were enzymatically dissociated and analyzed by flow cytometry for macrophage markers (A). The percentages of macrophages infiltrating the eye are shown (n = 5 per group) (B). (C, D) VEGF expression by macrophages at 3 days after laser was analyzed by flow cytometry. Representative histograms are shown (n = 5 per group) (C). Percentage of VEGF MFI was calculated in the indicated populations (D). Bars indicate means ± SEM. *$p < 0.05$, **$p < 0.01$, ***$p < 0.001$.
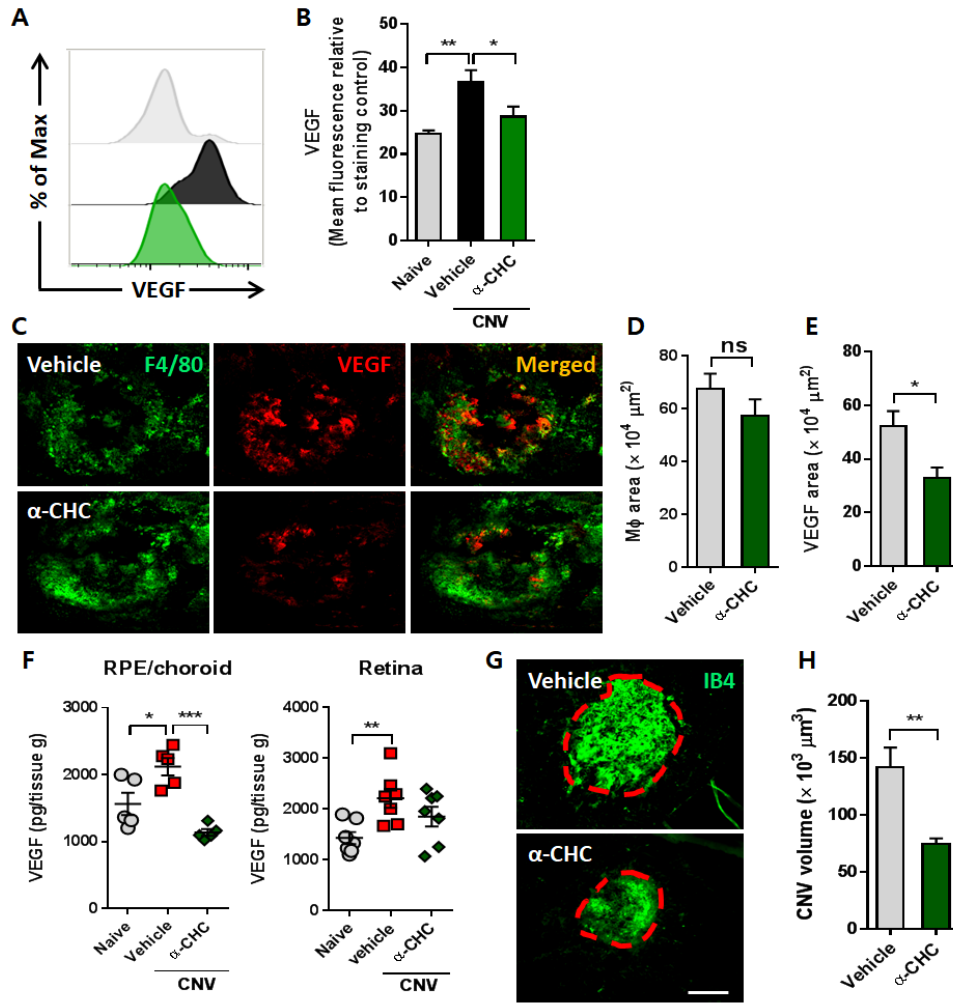
Figure 14. Blocking lactic acid uptake attenuates CNV. (A, B) Histogram (A) and quantitative graph (B) representing intracellular VEGF staining of macrophage in CNV mice received 2 μL 3 mM α-CHC or PBS intravitreally. Data obtained by flow cytometry. n =6. (C-E) Representative images of flat-mount choroidal tissue at 3 days after laser following PBS or 3 mM α-CHC injection were obtained by confocal immunofluorescence analysis using anti-F4/80 antibody (green) and anti-VEGF antibody (red) (C). Scale bar: 250 μm. Measurement of F4/80- (D) and VEGF- (E) stained area around the laser injury sites was performed using ImageJ software. (F) VEGF protein concentration in the RPE-choroid and retinal regions at 3 days after laser was

`

quantitatively measured with the ELISA technique. **(G, H)** Representative confocal images of IB4-stained RPE-choroid flat-mount. Tissues were obtained at 7 days after laser shot with PBS or 2 μL 3 mM α-CHC injection. The red dotted lines represent the edge of IB4-stained area (G). Quantitative graphs representing IB4-positive volumes (H). Bars indicate means $\pm$ SEM. $*p < 0.05$, $**p < 0.01$, $***p < 0.001$ determined by two-tailed paired t-test.

`
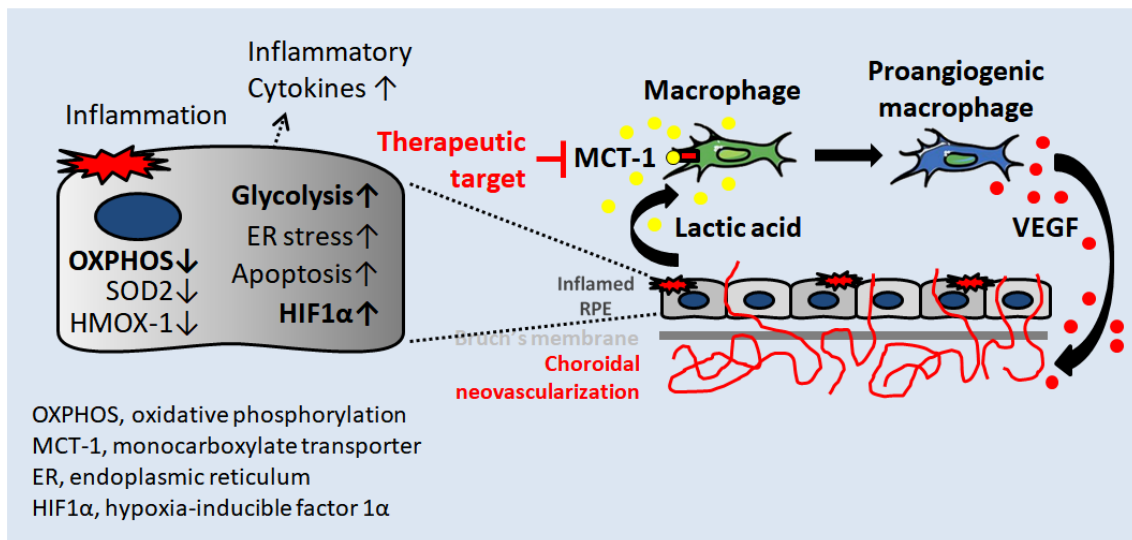
Figure 15. Schematic summary. Inflammation beyond homeostasis—maintaining parainflammation in the RPE results in metabolic alterations and subsequent pathobiolgical changes in the retinal microenvironment. In particular, lactic acid, a metabolic glycolytic end product possessing immune—modulating capacity, gradually increases in the retinal environment. In the development of CNV, macrophages uptake lactic acid though MCT1 and enhances VEGF secretion, facilitating neovascularzation. Interference of this lactic acid—induced signaling attenuates aberrant neovascularization. Thus, targeting macrophage metabolism is suggested as a promising strategy for CNV treatment.

6.4. DISCUSSION

The goal of this study was to create a global overview of inflammation-driven biological and metabolic alterations in RPE that causing destructive changes in the retinal environment, by using the latest tag-based multiplex proteomic/phosphoproteomic quantitative assay. To achieve this goal, a total of 4490 differentially expressed proteins and 1561 differentially phosphorylated proteins were identified in LPS-treated ARPE-19 cells. A significant downregulation of proteins related to mitochondrial respiration, cell cycle checkpoint, and the antioxidant system, the dysregulation of which were identified to be interconnected with robust perturbations in lipid metabolism, amino acid metabolism, ER stress, cell- matrix interaction, and apoptosis, was revealed. Early phosphorylation events associated with the MAPKK pathway, the Wnt/β-catenin pathway, and I-κB/NF-κB signaling, as well as subsequent phosphorylation/dephosphorylation of proteins related to cell aging, and cell- matrix adhesion, were identified to be involved in the pathogenesis. To my knowledge, this is the first large-scale proteome/phosphoproteome analysis of inflammation-triggered RPE cells in a human cell line, providing a comprehensive picture of the dynamically intertwined protein interaction network involved.

In addition, this study also revealed, for the first time, that a glycolytic end-product, lactic acid, increases VEGF production by macrophages to foster CNV development in the eye. There are several important findings to be discussed. First, an increase in lactic acid concentration was consistently observed in RPE-choroid tissues of an experimental CNV model. Second, lactic acid-

`

stimulated macrophages substantially enhanced tube formation of HUVECs, which was then diminished by α-CHC pretreatment. Third, blocking lactic acid transport by intravitreal injection of α-CHC into CNV mice significantly reduced VEGF expression in macrophage-infiltrated areas, total VEGF content in RPE-choroid tissues, and subsequent neovascularization.

Understanding the pathological mechanisms that damage the RPE during aging and disease has been challenging because of the lack of appropriate models that can faithfully recapitulate their multifactorial and complex pathobiology [38]. Hence, an integrated understanding based on the multiple models is recommended [38]. LPS, an agonist of toll-like receptor 4 (TLR4) used in this study for inducing inflammatory pathology, has frequently been utilized in RPE studies as a priming or stimulating agent as LPS-triggered downstream signals and the resulting phenotypes have been reported as similar to those observed in RPE pathobiology [39-44]. Interestingly, in the course of this study, an early and strong metabolic response after LPS challenge could be identified (Figures 1B-C), implying that subsequent metabolic overload of the mitochondria could occur, leading to various biological alterations. Indeed, after 24 h followed by the treatment with LPS, deeply interconnected perturbations in ER stress, cell-matrix adhesion, antioxidant mechanism, and apoptosis were observed (Figure 7).

This study presents a deep profiling of inflammation-driven phosphorylation events in RPE cells. At 45 min after LPS stimulation, multiple phosphorylation events, including that of SOS1 on Ser-1134, TRAF7 on Ser-61, MAP3K7 on Ser-389, and MAP3K11 on Thr-752 were identified (Figure 6), implying the subsequent activation of MAPK and NF-κB signaling pathways. In addition,

60
`

proteins involved in the Wnt/β-catenin pathway, such as BCL9 and SMARCA4, were also shown to be phosphorylated. These interconnected signaling pathways are implicated in a variety of signaling cascades wherein various extracellular stresses induce inflammation. Activation of the MAPK and NF-κB pathways and their involvement in the secretion of pro-inflammatory cytokines such as IL-6 and IL-8 has been reported previously in RPE cells after LPS stimulation [45, 46]. Increased phosphorylation of ERK 1/2 was also identified in inflamed and degenerative RPE during the pathogenesis of AMD and has been proposed as a potent therapeutic target [47]. Furthermore, the pathogenic role of Wnt/β-catenin signaling, via crosstalk with many other signaling pathways including NF-κB and HIF1α signaling, has been demonstrated in RPE-oriented degenerative disorders [48-50]. Considering the proteome and phosphoproteome data showing increased β-catenin expression along with elevated phosphorylation at residue Ser-552 upon LPS stimulation for 24 h (Figure 5B), Wnt/β-catenin signaling appears to be also activated in an inflammation-induced RPE model, whereas the expression of PI3K/Akt, which is known to phosphorylate β-catenin in a Wnt-independent fashion, was downregulated (Figure 5B). Instead, PRKAA2 (also known as AMPKα2) expression, another protein that can serve to phosphorylate β-catenin [51], was upregulated (Figure 5B), suggesting a possible crosstalk between AMPK and Wnt/β-catenin signaling pathways in inflammation-induced RPE. Phosphorylation of β-catenin on Ser-552 and its involvement in the activation of aerobic glycolysis for the production of pro-angiogenic factors have been previously described in various diseases such as cancer and AMD [52-54]. A similar β-catenin

61

`

phosphorylation response was observed during an oxidative stress−induced detrimental cellular dedifferentiation process in murine RPE [55]. In addition, activation of the Wnt/β−catenin pathway is known to induce VEGF, TNFα, and ICAM−1 in ARPE−19 cells [56].

In response to inflammatory stimuli, profound perturbations in mitochondria, lipid, and amino acid metabolic pathways were identified in RPE. Disturbances in metabolic stability have been implicated in inflammation and degenerative disease progression [57]. Mitochondria in the RPE are reportedly a primary site of pathology, especially in the context of aging [58]. Growing evidence has highlighted inflammation/oxidative stress−induced mitochondrial dysfunction and subsequent metabolic shifts from oxidative phosphorylation (OXPHOS) to glycolysis in RPE, thereby reducing the flow of glucose to photoreceptors, a process implicated in retinal degeneration [58−60]. In accordance with these studies, the results presented also showed strongly suppressed mitochondrial function with reduced levels of OXPHOS−related proteins such as ATP synthase (ATP5F1A−D), mitochondrially encoded cytochrome c oxidase (MT−CO1−3), and pyruvate dehydrogenase kinase (PDK1−3). My results showed an LPS−induced respiratory burst (Figure 1C), and substantial reduction of the mitochondrial antioxidant enzyme SOD2 (Figure 4B). Consequently, mitochondrial dysfunction is thought to be caused by elevated ROS levels within these mitochondria. SOD2 reduction and mitochondrial dysfunction have been reported in mice subjected to the light damage [61]. A positive correlation between SOD2 deficiency and the development of retinal degeneration has also been previously demonstrated [62, 63]. Although the molecular mechanism of inflammation−induced SOD2

`

reduction remains unknown, activated p53 signaling (Figure 4B) is suspected to be involved [64].

Previously, Winkler [65] reported that altered metabolic states induced by hyperglycemia and hypoxia resulted in human retinal lactate accumulation of 3- and 7-fold, respectively. In the case of AMD, pyruvate, lactate, and the corresponding lactate/pyruvate ratio were substantially increased in urine samples collected from typical AMD patients [20], suggesting that glycolysis may contribute to age-related microvascular alterations. The results of this study showing significant increases in lactic acid levels in laser-burned RPE-choroid complexes in mice might give insights into those findings from human AMD patients because I could prove that lactic acid accumulation is associated with CNV pathogenesis by potentiating macrophage-mediated VEGF secretion (Figure 9D). Although it is difficult to determine the exact levels of lactate in the subretinal space, they are presumed to be significantly elevated due to, at least in part, a glycolytic shift in damaged RPE-choroid cells. However, the possibility of lactic acid accumulation resulting from a blockade of the transport from retina to the choroid remains to be elucidated.

This study highlights an active role of lactic acid in macrophages during neovascularization. Administration of lactic acid at 20 mM significantly upregulated VEGF expression in human THP-1 macrophages, and promoted tube formation of HUVECs (Figures 10-12). Similarly, Zhu *et al.*[66] also demonstrated that an increase in retinal lactate by 30 mM in pathological states contributes to retinal VEGF production. It has also been reported that blood and muscle lactate levels can rise to concentration as high as 30 mM by extensive exercise [66, 67]. Considering that an eye features a lactate

`

concentration of 10 mM at normal steady-state, and that chronic inflammation and hypoxic stress may increase lactate levels, 20 mM of lactate is a realistic estimation of a concentration that could be expected to be found in the context of CNV pathogenesis [65].

The molecular mechanism of VEGF induction by lactic acid is thought to be related to the activation of the pH-sensing G protein-coupled receptor 132 (Gpr132, also known as G2A), which is highly expressed in macrophages [68-70]. In a GPR132-dependent manner, lactate-stimulated macrophages alternatively display an activated (M2) phenotype characterized by the expression of CD206 and arginase-1 [71]. The downstream molecule, HIF1α, which has been reported to be an essential mediator of M2 polarization of tumor-associated macrophages by tumor-derived lactic acid, is also suspected to be involved [72].

In this study, macrophage infiltration significantly increased at sites of neovascular lesions during CNV development (Figure 13). The data highlight elevated VEGF production by these macrophages, thus suggesting that macrophages potentiate the angiogenic capacity in CNV. This is consistent with previous reports showing that invading macrophages exhibit increased VEGF expression [73, 74]. Therefore, inhibition of CCR2 resulted in CNV suppression by reducing macrophage infiltration [75, 76]. The pro-angiogenic role of invading macrophages was also demonstrated by the attenuation of neovascularization after the removal of monocytes and macrophages following injection of clodronate liposome into CNV mice [77, 78]. These experimental results strongly imply a therapeutic potential for macrophage targeting strategies as part of CNV treatment approaches.

`

Although current options for AMD treatment including intravitreal anti-VEGF injection offer new hope for thousands of patients with neovascular AMD, there are risks of adverse effects, including severe atrophy of the choriocapillaris due to repeated treatments [79-81]. Instead, targeting macrophages to blunt excessive VEGF upregulation can be a promising strategy for future CNV therapy. A previous report showed that the inhibition of M2-type macrophage polarization by doxycycline holds the potential as an alternative therapeutic approach against long-term anti-VEGF treatments by attenuating IL-1β-induced pathological blood vessel growth [82]. Zandi et al. [83] also identified that inhibition of ROCK isoforms, which are associated with M2 shift, can reduce CNV incidence. In line with this, this study targeted the metabolic pathway network using the MCT1 blocker α-CHC to inhibit the pro-angiogenic activities of macrophages, suggesting that this may be an alternative or adjunct therapeutic approach to anti-VEGF treatment (Figure 14). Alpha-CHC has been used to inhibit lactic acid-induced signals promoting proliferation and migration in MCT1-expressing cells, such as endothelial and cancer cells [72, 84, 85]. For example, daily intraperitoneal injections of α-CHC blocked angiogenesis in Lewis lung carcinoma (LLC) tumors subcutaneously implanted into mice. In my study, lactic acid and α-CHC may have had direct effects on endothelial cell proliferation and neovascularization in CNV mice. Nevertheless, the experiments performed in this study using CNV mice showed a clear reduction of the VEGF signal proximal to macrophages, and led to attenuated neovascularization in response to α-CHC injection, demonstrating that lactic acid significantly impacts macrophage function in CNV development.

65

`

Collectively, I adopted the latest proteome and phosphoproteome profiling approach and applied it to a study on the pathobiology of RPE in response to overwhelming inflammation. Various concerted and integrated protein signals involved in the biological and metabolic responses triggered in ARPE-19 cells upon inflammation were presented. By layering the proteomic network tightly interwoven into the pathogenesis, I was able to identify numerous protein and phosphoprotein signatures possessing functional importance in RPE. In particular, I demonstrated that the glycolytic by-product lactic acid accumulates in the CNV microenvironment, where it contributes to neovascularization through a pro-angiogenic shift of the infiltrating macrophages. From a therapeutic point of view, these findings imply that functional modulation of macrophages should be considered as the future therapeutic applications in CNV.

`

Finding a Macrophage Targeting Strategy in Cancer

; Macrophages are essential to FIH−G9a axis− induced ovarian cancer metastasis

`

7.1. INTRODUCTION

Cooperation among different cellular and non-cellular elements defining the tumor microenvironment facilitates cancer development and metastasis [86]. Tumor-associated macrophages (TAMs), highly abundant immune-related stromal cells in the tumor microenvironment, are key orchestrators of these processes, directly facilitating tumor growth, angiogenesis, extracellular matrix (ECM) remodeling, and metastasis [87-89]. In fact, growing clinical and experimental evidence suggests that metastasis occurs when primary tumors are too small to be detected by diagnostic tools, and that recruited monocytes and differentiated TAMs play a key role during early dissemination [90, 91]. However, due to the difficulties in visualization and investigation of early events of cancer cell dissemination, and the lack of an appropriate and optimal preclinical model, dissecting the multifaceted contribution of monocytes and TAMs in early metastasis remains a challenging task.

G9a, euchromatin-localized histone methyltransferase 2 (EHMT2), is an epigenetic regulator primarily responsible for the dimethylation of histone H3 lysine 9 (H3K9), generally resulting in specific gene repression [92]. Although it is a critical regulator of cellular differentiation during embryonic development [93, 94], G9a has also been shown to play an important role in tumor progression and metastasis [95]. Indeed, many reports have demonstrated an upregulation of G9a expression in various human cancers including colon, breast, liver, lung, prostate, and bladder cancers as well as lymphoma, and highlighted its pro-tumorigenic and pro-metastatic properties [95-98]. A recent study also revealed that G9a is regulated by an upstream

`

regulator, factor inhibiting HIF (FIH), which hydroxylates and inhibits G9a under normoxia while the FIH reaction is limited under hypoxia [99]. Due to its epithelial−to−mesenchymal transition (EMT)−promoting effect, the FIH−G9a pathway was suggested as a potential target for inhibiting hypoxia−induced cancer metastasis [99]. Given that cancer cells having undergone EMT modulate the tumor microenvironment in favor of tumor survival, the FIH−G9a axis in cancer cells is also thought to play an important role in fostering the tumor microenvironment and facilitating early cancer dissemination.

The zebrafish has garnered considerable attention as a powerful model system for studying human cancer because of the following advantages: (ⅰ) its immune−privileged nature without inducing rejection of implanted human or mouse cells, (ⅱ) ease of genetic manipulation, (ⅲ) availability of transgenic zebrafish strains such as the Tg(*mpeg1*:dendra2) strain allowing visualization of cellular interactions, and (ⅳ) transparent embryos enabling single cell−based observation [91, 100]. In addition, innate immune cells are present at the time of xenotransplantation, whereas the adaptive immune system has not yet been developed, thereby providing an outstanding opportunity to study cancer cell interactions specifically with innate immune cells in vivo [101].

Here, by using a zebrafish metastasis model and adopting the human ovarian cancer cell line SKOV−3, in which the expression of FIH−G9a was modulated, I sought to elucidate the effect of the FIH−G9a axis of ovarian cancer cells on the tumor microenvironment, especially on monocytes and TAMs, during early metastatic processes. In this study, I have revealed the FIH−G9a axis−dependent interactions between cancer cells and macrophages, which facilitate

`

cancer cell dissemination. Moreover, I could unravel FIH-G9a axis-dependent monocyte recruitment and macrophage activation. Through secretome analysis, FIH-G9a axis-induced protein changes fostering a cancer-favorable tumor microenvironment were profiled. The results presented here are expected to have profound implications in providing a better understanding of early metastatic progression, and in developing therapeutic intervention strategies for various cancers.

`

7.2. MATERIALS AND METHODS

Zebrafish Tumor Model

All zebrafish experiments were approved by the Seoul National University Animal Care and Use Committee (Approval No. SNU-171017-7-2). The transgenic zebrafish lines Tg(*Fli1*:EGFP), Tg(*mpeg1*:dendra2), and Tg(*mpx*:mcherry) were raised at 28℃ under standard experimental conditions. Twenty-four hours post fertilization (hpf) zebrafish embryos were incubated in aquarium water containing 0.2 mmol/L 1-phenyl-2-thio-urea (PTU, Sigma) to prevent pigmentation. At 48 hpf, embryos were dechorionated with a pair of sharp-tip forceps and anesthetized with 0.04 mg/mL of tricaine (MS-222, Sigma). Anesthetized embryos were moved onto a modified agarose gel for microinjection. Before injection, tumor cells or macrophages were labeled in vitro with Vybrant DiD or DiI cell-labeling solution (Life Technologies). Approximately 300-500 tumor cells or a mixture of equal numbers of 150-250 tumor cells and 150-250 macrophages were resuspended in serum-free DMEM (Gibco) and 5 nL of tumor cell solution were injected into the perivitelline space (PVS) of each embryo by an Eppendorf microinjector (FemtoJet 5247, Eppendorf, Hamburg, Germany). Nonfilamentous borosilicate glass capillaries needles were used for the injection. After injection, the zebrafish embryos were immediately transferred into PTU aquarium water. Injected embryos were kept at 28℃ and were checked 3 days after injection for investigating tumor invasion and metastasis using a fluorescent microscope (CTR6000, Leica, Wetzlar, Germany).

`

Cell Culture

Human ovarian cancer cell line SKOV-3 expressing G9a or N799Q mutant were kindly provided by Professor Jong-Wan Park. They were cultured in RPMI1640 supplemented with 10% FBS (Gibco) and 1% penicillin-streptomycin (Gibco) and grown in a humidified atmosphere containing 5% CO_2 at 37℃. Human acute monocytic leukemia THP-1 cell line was maintained in RPMI media containing 10% FBS (Gibco) and differentiated into macrophages by incubation with 100 nM PMA (Sigma) for 24 h at 37℃ with 5% CO_2.

Isolation and Differentiation of Bone Marrow-derived Macrophages (BMDM)

Bone marrow cells were obtained from C57BL/6J male mice of 7-12 wks of age and differentiated for 7 days in RPMI 1640 media containing 10% FBS, 1% penicillin/streptomycin, and 2 mM of L-glutamine (Gibco), supplemented with fresh recombinant murine M-CSF (25 ng/ml; Miltenyi Biotec) every three days, into bone marrow derived macrophages (BMDMs). Cells were cultured at 37℃ in a humidified incubator containing 5% CO_2.

Lentiviral Infection

The lentiviral G9a shRNA constructs were purchased from Dharmacon (RHS4533-EG10919, Dharmacon Research, Chicago, IL, USA). The FIH shRNA construct was kindly provided by Professor Jong-Wan Park. Lentiviruses were produced by transfecting into 293FT cells by using the Lentivral packaging kit (OriGene, Rockville, MD, USA). Viral supernatants were harvested and used to infect SKOV-3 Control or G9a-WT cells with 8

`

μg/mL polybrene. Cells were selected using 1.5 μg/mL puromycin and used for the downstream experiments.

Zebrafish Morpholino Injection

Pu.1 morpholino oligonucleotide was purchased from Gene Tools, LLC (Corvalis, OR, USA). The morpholino oligomer target sequences were from 5′ to 3′, as follows: Pu.1 MO: GATATACTGATACTCCATTGGTGGT, Con MO: CCTCTTACCTCAGTTACAATTTATA. For Pu.1 knockdown as previously published [102, 103], 1 mM Pu.1MO was injected into 1−4 cell embryos, as described [104]. Embryos from the same matings were injected with an equal volume of phenol red/nuclease−free water mixture as a control and some embryos served as uninjected controls.

Western Blotting

The cells were harvested with the 1X sample buffer (Biosesang) containing a protease inhibitor and phosphatase inhibitor cocktail (GenDepot). The total cell lysates were sonicated for 30 sec and heated to 100℃ for 10 min. The proteins were separated on 8% polyacrylamide gels followed by transfer onto polyvinylidene difluoride (PVDF) membranes (Merck Millipore). Mouse anti−FIH (A−5; Santa Cruz Biotechnology Inc.), rabbit anti−G9a/EHMT2 (C6H3; Cell Signaling Technology), and mouse anti−β−actin (Santa Cruz Biotechnology Inc.) were used at 1/2000 dilutions.

RNA Isolation and Real−Time RT−PCR

`

Total RNA was extracted from cells with Trizol (Invitrogen) following the manufacturer's instructions. RNA concentration/quality was assessed by NanoDrop spectrophotometer (NanoDrop Technology). Equal amounts of RNA were reverse transcribed into cDNA with Reverse Transcription kits (Enzynomics) and gene expression was determined by quantitative real-time PCR using SYBR Green PCR Master Mix (Applied Biosystems) on an ABI PRISM 7900 (Applied Biosystems). The relative mRNA expressions of each sample were normalized by β-actin and Student's unpaired t-test was used for statistical analysis. Sequences of primers used for amplifications were as follows: β-actin: FP, 5'-ATTGCCGACAGGATGCAGAA-3'; RP, 5'-GCTGATCCACATCTGCTGGAA-3'; FIH: FP, 5'- GCCAGCACCCACAAGTTCTT-3'; RP, 5'- CCTGTTGGACCTCGGCTTAA-3'; G9a: FP, 5'-CATTTCCGCATGAGTGATGATGT-3'; RP, 5'- GGCAGAACCTAACTCCTCCGA-3'.

Transswell Migration Assay

Cancer cells were seeded onto a 12-well plate at a density of 8.0×10^5 on day 0, and the culture supernatants were harvested on Day 2. A total of 600 μL of supernatant was applied to the bottom of the Transwell chamber. This was followed by the addition of 250 μL of 5×10^4 THP-1 monocytes on the top of the polycarbonate membrane inserts ($8-\mu$m-pore-size, Corning). After 4-6 h incubation at 37℃ in a CO_2 incubator, the inserts were transferred to a new 24-well plate. The top of the insert membrane was washed with a cotton swab, and 1 ml of methanol was used to fix the cells for 5 min at room temperature. After washing with PBS, the membranes were stained with hematoxylin for 8 min and eosin for 30 sec. After washing with

`

PBS, finally, the membranes were dried and scanned underneath the membranes using a light microscopy (Labophot; Nikon)

Immunofluorescence Staining

After fixed with 4% paraformaldehyde for 15 min at room temperature, THP-1 macrophages were washed with PBS containing 0.3% Triton X-100 (PBST) three times and blocked at 37℃ for 1 h in PBST supplemented with 5% FBS (Gibco). Then, the cells were incubated with the following primary antibody at 4°C overnight: mouse anti-CD206 (BioLegend, San Diego, CA, USA). Cells were washed 3 times for 5 min with PBST and incubated with Alexa Fluor 635-labeled goat anti-mouse IgG (Molecular Probes) and DAPI for 1 h at room temperature. Stained cells were examined under Olympus FV1000 Confocal Scanning Scope (Olympus).

Flow Cytometry

THP-1 cells differentiated with 100nM PMA for 24 h were treated with cancer supernatant for 3 days. After fixation, cells were stained with PE-conjugated anti-CD206 (clone: MR6F3; eBioscience). Labeled cells were analyzed using LSR-II cytometer (BD Biosciences), and the data were analyzed using FlowJo Software (version 7.6.2).

Wound Scratch Assay

SKOV-3 control cells were seeded onto a 24-well plate at a density of 10^5 and allowed to achieve 95% confluency. Then, a scratch extending the length of each well was made using a standard 200 μL pipette tip. After washed with

`

PBS solution, THP-1 conditioned media (CM) harvested with the addition of 1% FBS for 24 h was treated. The plate was incubated at 37℃ in 5% CO_2 for 24 h and media was not changed during this time. Three photomicrographs of each scratch were obtained at the initial time of wound creation and the same location was photographed every 6 h thereafter until completion of the study. Image analysis software (ImageJ) was used to quantify the area of the wound remaining. This number was then converted to a percentage of the wound closure at each time point.

Preparation of CM for Secretome Analysis

SKOV-3 control or G9a-NQ cells were seeded onto a 100-mm dish tissue culture plate (2×10^6 cells per well; Corning) and incubated with 10 mL of serum-free RPMI1640 for 48 h in a humidified chamber kept at 37℃ in 5% $CO_{2.}$ The CM was harvested and centrifuged at 3,000 rpm for 10 min to remove large particulates. Then, the CM was concentrated to about 400 μL by ultrafiltration (3-kDa cutoff membrane; Amicon Corporation, Danvers, MA, USA). The CM was stored at -80℃ for the downstream secretome analysis.

Nano LC-MS/MS analysis

LC-MS/MS analysis methods were performed using Quadrupole Orbitrap mass spectrometers, Q-exactive plus (Thermo Fisher Scientific) coupled to an Ultimate 3000 RSLC systems (Dionex, Sunnyvale, CA, USA) with a nano electrospray source as previously described with some modifications [105, 106]. Peptide samples were separated on the 2-column setup with a trap column (75 μm I.D. $\times$ 2 cm, C18 3 μm, 100 Å) and an analytical column

`

(50 μm I.D. $\times$ 15 cm, C18 1.9 μm, 100 Å). Prior to sample injection, the dried peptide samples were redissolved in solvent A (2% acetonitrile and 0.1% formic acid). After the samples were loaded onto the nano LC, a 90-min gradient from 8 to 30% solvent B (100% acetonitrile and 0.1% formic acid) was applied to all samples. The spray voltage was 2.0 kV in positive ion mode and the temperature of the heated capillary was set to 320℃. Mass spectra were acquired in data-dependent mode using a top 15 method on a Q Exactive. The Orbitrap analyser scanned precursor ions with a mass range of 300-1650 m/z and resolution of 70,000 at m/z 200. Higher-energy collisional dissociation (HCD) scans were acquired on the Q Exactive at a resolution of 17,500. HCD peptide fragments were acquired at a normalised collision energy of 28. The maximum ion injection times for the survey and MS/MS scans were 20 and 120 ms, respectively.

Bioinformatics Analysis

Statistical analysis for nano LC-MS/MS data was performed using the Perseus software [31]. Protein quantification data was analyzed using gene set enrichment analysis (GSEA) by ranking gene products according to a differentiability statistic using GSEA's Molecular Signature Database and shown with density plots depicting the abundance of a gene set relative to the entire dataset (https://www.gsea-msigdb.org/gsea/msigdb/collections.jsp).

Multiplex Membrane-based Immunoassay

SKOV-3 control or G9a-NQ cells were seeded onto a 6-well cell culture plate (1.6 $\times$ 10^5 cells per well; Corning) and incubated with serum-free

`

RPMI1640 for 24 h in a humidified chamber kept at 37℃ in 5% CO_2. The CM was harvested and centrifuged at 3,000 rpm for 10 min to remove large particulates. Then, the human cytokine array (ARY005, R&D Systems, MN, USA) was conducted according to the manufacturer instructions.

Statistical Analysis

All statistical analyses were run using GraphPad Prism 6.07 software and displayed as the mean $\pm$ S.E.M. The statistical significance of the difference was assessed using Student t-test. A significant difference was considered when the p-value was less than 0.05 and was represented by *, $p < 0.05$, **, $p < 0.01$ and ***, $p < 0.001$, ****, $p < 0.0001$.

`

7.3. RESULTS

Establishment of a multicolor-based system to monitor interaction between cancer cells and macrophages

To recapitulate the tumor microenvironment and visualize the cancer cell and macrophage interactions, I took advantage of human-in-fish xenotransplantation. This approach has been reported as a powerful tool to explore interactions between tumor cells and microenvironmental components [107-110]. In this system, DiD dye-labeled human cancer cells were implanted into the perivitelline space (PVS) (Figure 1A). Macrophages were also labeled with DiI dye as a non-overlapping color. These DiD-labeled cancer cells and DiI-labeled macrophages were coimplanted into PVS of the same zebrafish and interactions between these cell types could be kinetically monitored in the living zebrafish body, as described previously [91]. Moreover, injection of color-labeled cells into the transgenic *mpeg1*:dendra2 zebrafish that labels macrophages and into the transgenic *Fli1*:EGFP zebrafish that labels vascular endothelial cells allowed us to study the complex interactions between three important cellular components in the tumor microenvironment, that is, tumor cells, macrophages, and vascular endothelial cells (Figures 1B-D). Thus, this multiple color system, in part, recapitulates the tumor microenvironment and provides a unique opportunity to investigate interactions between various cellular components in primary tumors in facilitating cancer metastasis.

`

Macrophages are associated with ovarian cancer cells during metastasis in G9a-dependent manner

To visualize and investigate the interaction between cancer cells and macrophages, SKOV-3 control cells were implanted into the PVS in Tg(*mpeg1*:dendra2) zebrafish embryos (Figure 2A). I observed that host macrophages were recruited around to the cancer cells within 1 hour after implantation and make dynamic cellular interaction with human cancer cells (Figure 2B). The macrophages and tumor cells overlapped their fluorescent membranes and were in close proximity with one another. In particular, the close interaction between cancer cells and macrophages during intravasation process was also observed by the time-lapse confocal imaging, suggesting the active role of macrophages in cancer cell intravasation during metastasis (Figure 2C).

I then wondered whether cancer cell-macrophage interaction is dependent of G9a of cancer cell. I established the SKOV-3 control cells deficient with G9a expression by infecting lentivirus containing G9a shRNA (Figures 3A-B) and implanted into the Tg(*mpeg1*:dendra2) zebrafish embryos. As shown in figures 3D-E, the metastasis was significantly suppressed by G9a knockdown. Interestingly, the overlap signal of cancer cells and macrophages was also reduced by G9a knockdown, suggesting the positive correlation between G9a of cancer cells and interaction with macrophages (Figures 3F-G).

Macrophages are associated with ovarian cancer cells during metastasis in FIH-G9a axis-dependent manner

`

To further demonstrate the hypothesis that G9a governs cancer cell-macrophage interaction during metastasis, I adopted the SKOV-3 cell lines expressing G9a or N799Q mutant ("NQ mutant", kindly provided by Professor Jong-Wan Park). Further, I established the SKOV-3 G9a-WT cells deficient with FIH expression by infecting lentivirus containing FIH shRNA (Figures 4A-B). This is because FIH has been previously reported as an upstream regulator of G9a, which hydroxylates and inhibits G9a under normoxia [99]. Then, I implanted the SKOV-3 control, G9a-WT/sh-EGFP, G9a-WT/sh-FIH, and G9a-NQ cells into the Tg(*mpeg1*:dendra2) zebrafish embryos, respectively, and examined the interactions during metastatic cascade. Intriguingly, the total number as well as percentage of cancer cells coupled with macrophages increased significantly in proportion to the increase of FIH-G9a expression. These results show that the interaction between cancer cells and macrophages occurs through FIH-G9a axis-dependent mechanism of cancer.

Myeloid cells depletion reduces metastasis of SKOV-3 cells

These preclinical findings promoted me to study if macrophages are necessary in FIH-G9a axis-dependent dissemination of cancer. To test the role of macrophages during early metastasis, I adopted morpholino (MO) oligonucleotides to knockdown the transcription factor Pu.1, which controls the development and differentiation of myeloid cells in zebrafish embryos [102]. As previously described, Pu.1 knockdown is most effective in suppressing macrophage differentiation, while neutrophil differentiation can be suppressed only under maximal knockdown conditions [103]. As shown in

81

`

figure 6, macrophages and neutrophils were clearly visible from about 20 hpf in transparent zebrafish embryos (Figure 6). In agreement with previous reports, in my experiments macrophages were depleted in zebrafish embryos up to 72 hpf, while neurophils were unaffected by 1 mM Pu.1 MO injection (Figures 7, 8A). Interestingly, in Pu.1 MO-injected larvae, cancer cell dissemination of SKOV-3 G9a-NQ cells is substantially reduced (Figure 8B). In addition, it is observed that cancer cell dissemination started after 2 dpi, when macrophages were generated to normal ranges, and the FIH-G9a-regulated cancer cells were more affected by the presence of macrophages (Figure 8C). These results strongly imply that macrophages are critical in FIH-G9a axis-dependent cancer dissemination.

FIH-G9a axis of cancer cells activates macrophages to M2-like phenotype

Next, I asked whether monocytes are recruited by FIH-G9a axis dependent manner. To investigate this, conditioned media (CM) from SKOV-3 control, G9a-WT, G9a-WT/sh-FIH, and G9a-NQ cells were collected and subjected to monocyte migration assay. As shown in figure 9A, CM from G9a-NQ cells showed significantly increased the numbers of migrated monocytes. To further identify the effect of FIH-G9a axis on macrophages, I treated the each CM onto the THP-1 macrophages and examined the morphological changes. THP-1 macrophages stimulated with CM from G9a-NQ showed extended and bipolar phenotype compared to those of untreated controls (Figure 9B). The CD206 expression of THP-1 macrophages was also significantly upregulated by the CM from the G9a-NQ cells (Figure 10), suggesting that FIH-G9a axis of cancer cells enhances M2-like phenotypes in macrophages.

`

Activated macrophages facilitate metastasis of ovarian cancer cells

To investigate whether activated macrophages actually enhance cancer cell metastasis, the CM from THP-1 macrophages stimulated with supernatants from SKOV-3 control, G9a-WT, G9a-WT/sh-FIH, and G9a-NQ cells were harvested and subjected to wound scratch assay in SKOV-3 control cells. As shown in figure 11A, the CM from G9a-NQ supernatant-treated THP-1 macrophages substantially potentiated the mobility of SKOV-3 control cells. To further confirm the metastasis-promoting ability of activated macrophages, activated macrophages were coimplanted with SKOV-3 control cells into Tg(*Fli*:EGFP) zebrafish embryos, and their abilities in facilitating metastasis were analyzed. The SKOV-3 control cells coinjected with G9a-NQ-stimulated THP-1 macrophages showed increased metastasis compared to those in single injection or coinjection with control supernatant-treated THP-1 macrophages (Figure 11B). Further, to exclude the effect of zebrafish macrophages on metastasis and examine the genuine role of coinjected macrophages, macrophage-depleted zebrafish embryos were also adopted coimplantation experiments, and mouse bone marrow-derived macrophages (BMDM) stimulated with supernatants from SKOV-3 control, G9a-WT, G9a-WT/sh-FIH, and G9a-NQ were coimplanted with SKOV-3 control cells. BMDMs stimulated with G9a-NQ enhanced the dissemination of coimplanted SKOV-3 control cells (Figure 12). These results suggest that FIH-G9a axis of cancer cells activates macrophages to pro-metastatic phenotype.

Differential protein secretome analysis in SKOV-3 control and NQ cells

`

To identify the proteins secreted by the FIH-G9a dependent manner in cancer cells and fostering tumor microenvironment, I performed the nano LC-MS/MS to identify differentially secreted proteins between SKOV-3 control and G9a-NQ cells. I performed gene set enrichment analysis (GSEA) of differentially secreted protein data set (FDR < 0.25) by raking gene products according to a differentiability statistic using GSEA's Molecular Signature Database (http://www.gsea-msigdb.org/gsea/msigdb/collection.jsp) (Figure 13). A heat map revealed that the majority of genes involved in 'pathway in cancer', 'cell adhesion molecules', 'ECM receptor interaction', and 'endocytosis' were upregulated by G9a overexpression. In particular, pro-tumorigenic and pro-metastatic cytokines including TGFβ1, VEGFA, and PDGFC were identified as upregulated in G9a-NQ compared to those in control cells. In addition, since highly bioactive proteins such as growth factors and chemokines are often secreted at very low levels and usually not detected by proteomic analysis [111, 112], I supplemented my nano LC-MS/MS with human cytokine array. As shown in figure 14, pro-tumorigenic cytokines such as CXCL1, IL-8, and SerpinE1 were elevated in CM of G9a-NQ compare to control cells.

Collectively, I revealed that FIH-G9a axis in ovarian cancer cells governed the secretion of pro-tumorigenic and pro-metastatic cytokines including TGFβ1, VEGFA, PDGFC, CXCL1, IL-8, and SerpinE1. Due to these factors, monocyte recruitment and differentiation to CD206-positive macrophages were significantly upregulated. Reciprocally, activated macrophages resulted in enhancement of cancer cell migration and metastasis, forming a positive feedback loop. Therefore, targeting this loop fostered by FIH-G9a axis in

`

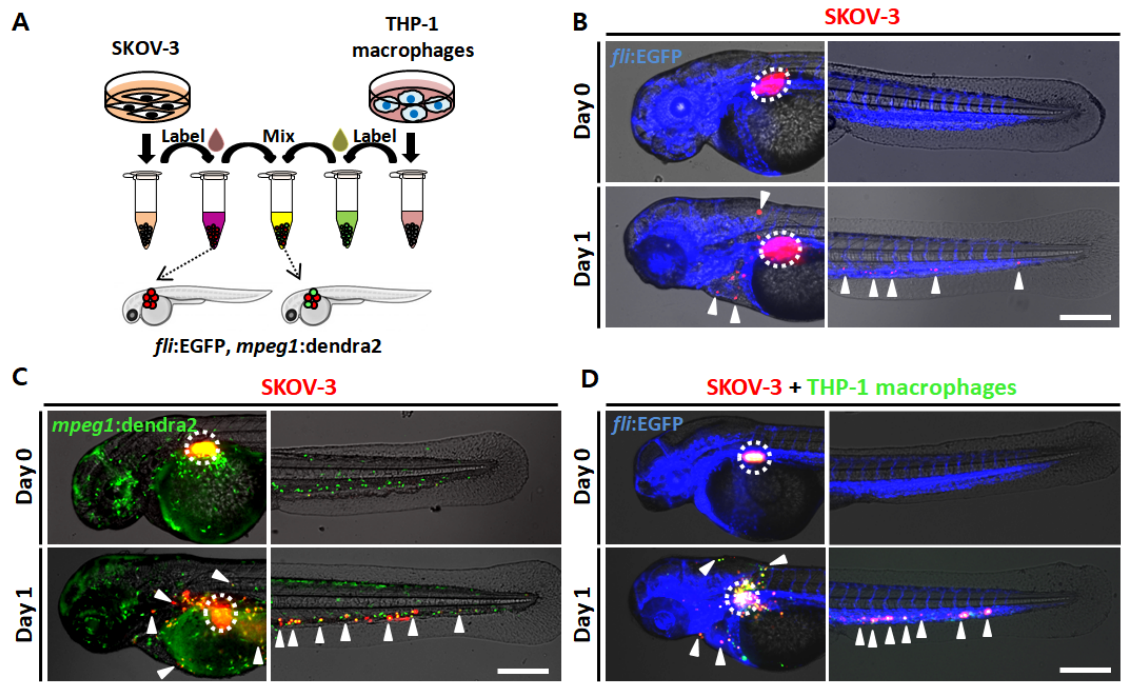cancer is suggested as a promising therapeutic strategy against cancer metastasis.

`

Figure 1. Establishment of a multicolor-based system to monitor interactions between cancer cells, macrophages, and microvessels. (A) Schematic overview of implantation of human ovarian cancer cell line SKOV-3 and macrophages. Cultured monolayers of cancer cells and THP-1 macrophages were harvested and labeled with different colors. The labeled cells were implanted into the perivitelline space (PVS) of each zebrafish embryos. (B-D) Representative fluorescence images of cancer cell dissemination in Tg(*Fli1*:EGFP) (B) and Tg(*mpeg1*:dendra2) (C), and the cancer cell-macrophage complex dissemination in *Fli1*:EGFP (D) after 1 day postimplantation. White arrowheads point to disseminated and metastatic cancer cells. Scale bar; 250 μm.
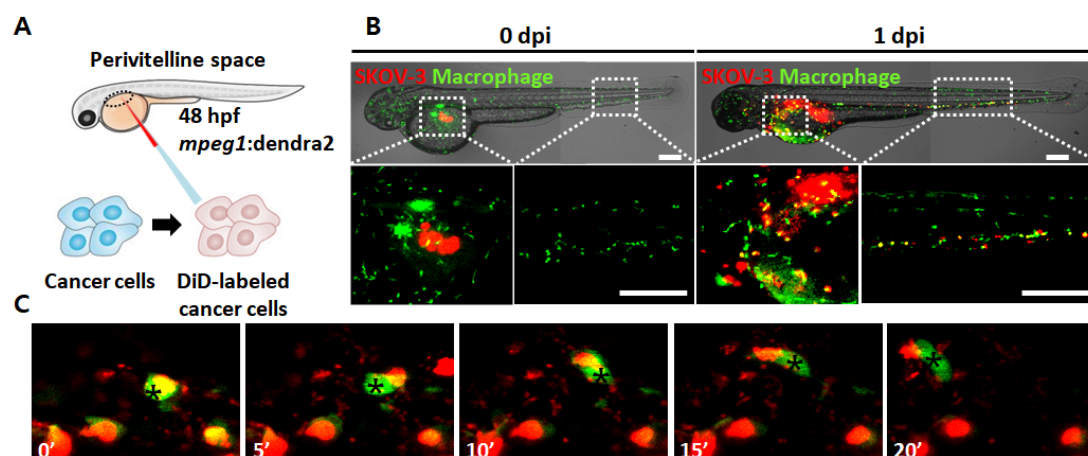
`

Figure 2. Macrophages interact with cancer cells during metastasis. (A) Schematic diagram of implantation of SKOV−3 cells in *mpeg1*:dendra2 zebrafish embryo. (B) Representative fluorescence images showing immediate monocytes recruitment and their close interaction with cancer cells during metastasis of SKOV−3 cells. (C) Still images from time−lapse video of SKOV−3 cells (red), 5 sec time interval, revealing dynamic interaction with zebrafish macrophages (green) during intravasation process. Zebrafish macrophage is marked by the black asterisk. Scale bar; 250 μm.
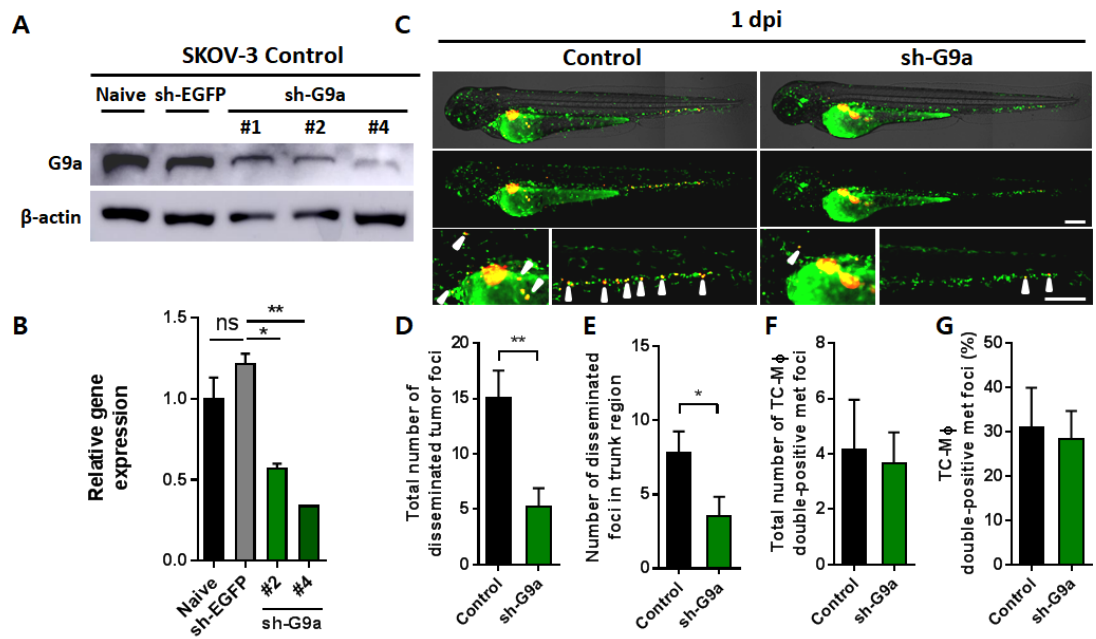
`

Figure 3. Macrophages are associated with ovarian cancer cells during metastasis in G9a axis-dependent manner. (A-B) Stable knockdown of G9a in SKOV-3 control cells. The expression was examined by western blotting (A) and real-time qPCR (B). SKOV-3 control cells expressing G9a shRNA #4 were used for the downstream experiment. (C) Examination of the implanted DiI-labeled SKOV-3 control and sh-G9a cells on day 0 and day 1 after implantation in *mpeg1*:dendra2 zebrafish embryos. White arrowheads point to disseminated and metastatic cancer cells. (D) Quantification of the total number of disseminated tumor foci in SKOV-3-bearing zebrafish embryos (n = 20 embryos/group). (E) Quantification of the number of disseminated tumor foci in the trunk region of SKOV-3-bearing zebrafish embryos (n = 20 embryos/group). (F) Quantification of the total number of the disseminated tumor foci overlapping zebrafish macrophages (n = 20 embryos/group). (G) Quantification of the percentage of the disseminated tumor foci overlapping zebrafish macrophages (n = 20 embryos/group). Quantification was analyzed

`

at day 1 after tumor implantation. Scale bar; 250 μm. Data represent mean $\pm$

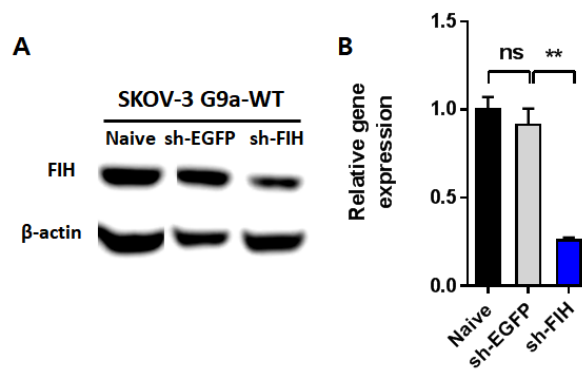S.E.M. $*p < 0.05$, $**p < 0.01$ by Student's t-test. NS, nonsignificant.

`

Figure 4. Stable knockdown of FIH in SKOV−3 G9a−WT cells. (A) The protein expression of FIH in SKOV−3 G9a−WT cells stably expressing control shRNA or FIH shRNA. **(B)** The mRNA expression of FIH in SKOV G9a−WT cells stably expressing control shRNA or FIH shRNA. Data represent mean ± S.E.M. $*p < 0.05$, $**p < 0.01$ by Student's t−test. NS, nonsignificant.
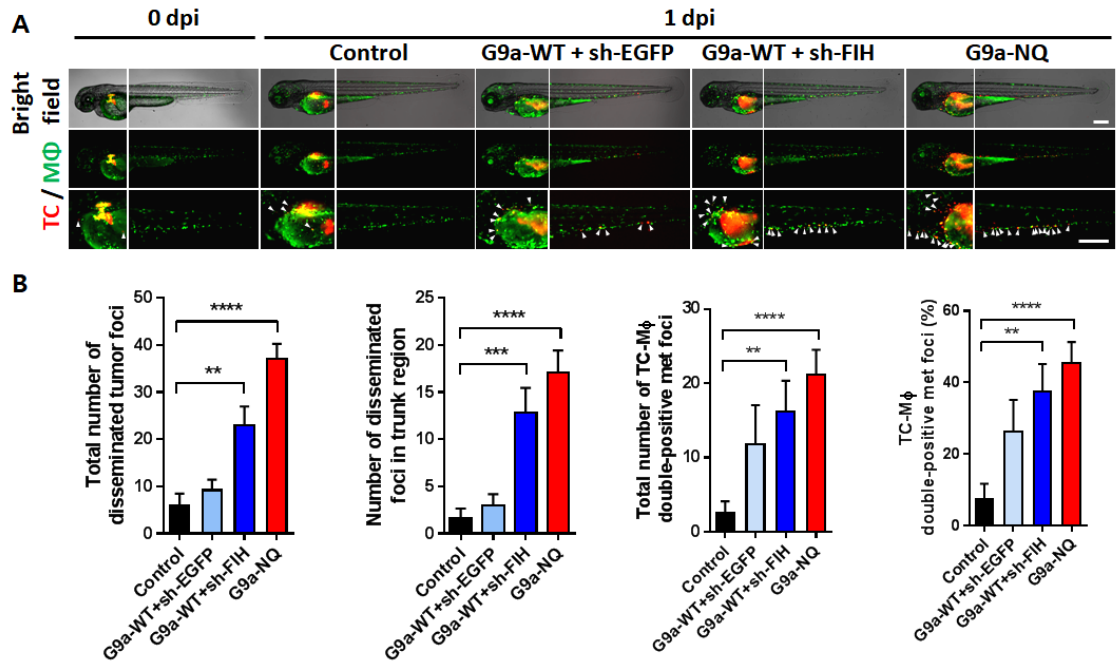
`

Figure 5. Macrophages are associated with ovarian cancer cells during metastasis in FIH–G9a axis–dependent manner. (A) Examination of the implanted DiI–labeled SKOV–3 control, G9a–WT, G9a–WT+sh–FIH, and G9a–NQ cells on day 0 and day 1 after implantation in *mpeg1*:dendra2 zebrafish embryos. White arrowheads point to disseminated and metastatic cancer cells. (B) Quantification of the total number of disseminated tumor foci, the number of disseminated tumor foci in the trunk region, the total number of zebrafish macrophages–TC double positive metastatic foci, and the percentage of the disseminated zebrafish macrophages–TC double positive metastatic foci in zebrafish embryos implanted with FIH–G9a axis–overexpressing SKOV–3 cells (n = 15~20 embryos/group). Scale bar; 250 μm. Data represent mean $\pm$ S.E.M. **$p < 0.01$ ***$p < 0.001$, ****$p < 0.0001$ by Student's t–test.

`

A Caudal hematopoietic tissue (CHT)

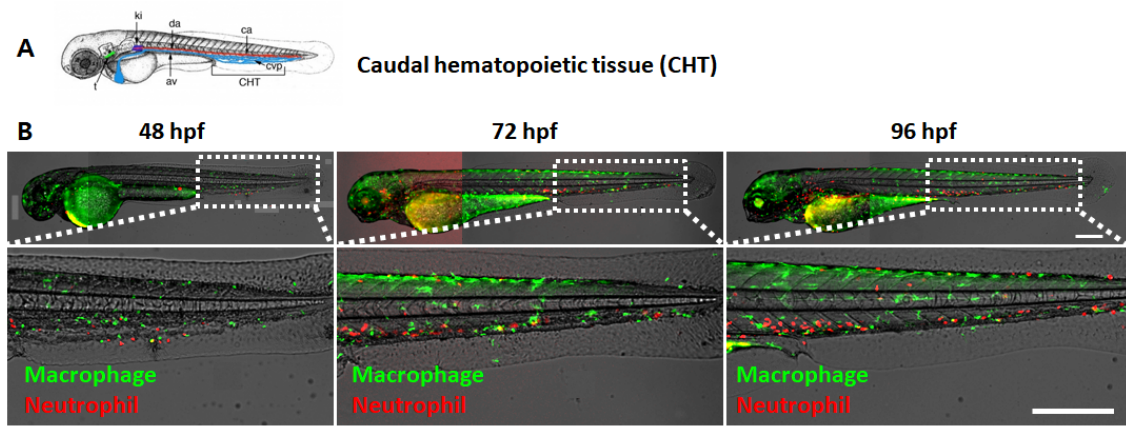**B** 48 hpf 72 hpf 96 hpf

Macrophage
Neutrophil

Figure 6. Characterization of macrophages and neutrophils in the region of CHT in developing zebrafish embryo. (A) Schematic showing the region of caudal hematopoietic tissue (CHT) in zebrafish embryo (B) Representative fluorescence images showing macrophages (green) and neutrophils (red) in the region of CHT in developing Tg(*mpeg1*:dendra2/*mpx*:mcherry) zebrafish embryo. Scale bar; 250 μm.
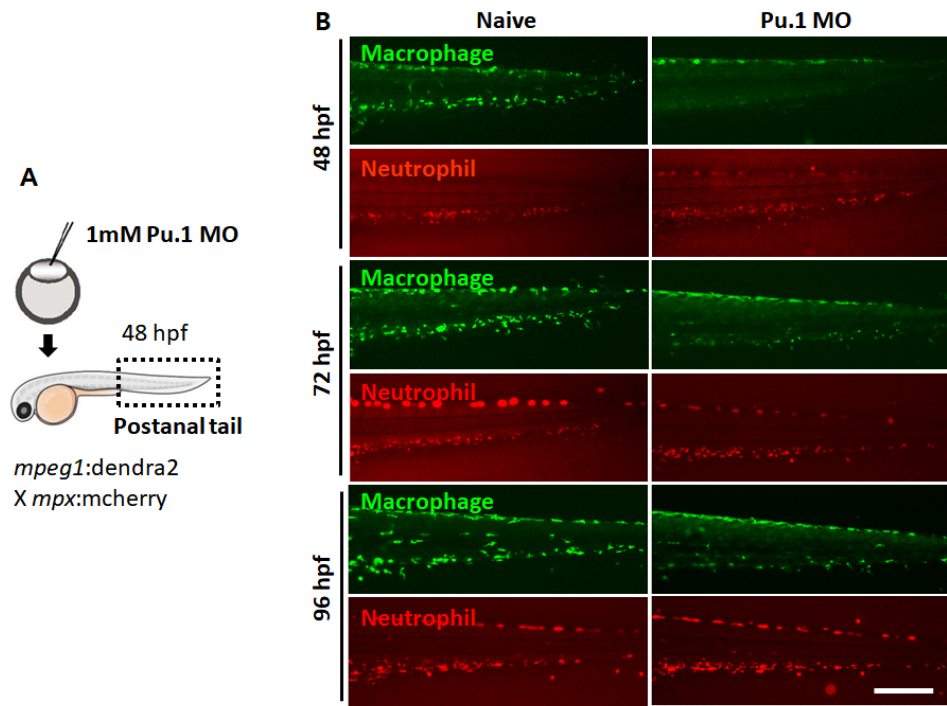
`

Figure 7. Lineage-specific depletion of macrophages by the morpholino-mediated knockdown of Pu.1. (A) Illustration of the experiment for the depletion of macrophages in zebrafish embryos. 1 mM Pu.1 MO was injected into the 1-4 cell stage of Tg(*mpeg1*:dendra2/*mpx*:mcherry) embryos. (B) Representative fluorescence images showing suppressed differentiation of macrophage (green) at 48 hpf in MO-injected embryos. The differentiation of neutrophils (red) was unaffected by the injection of 1 mM Pu.1 MO. Scale bar; 250 μm.
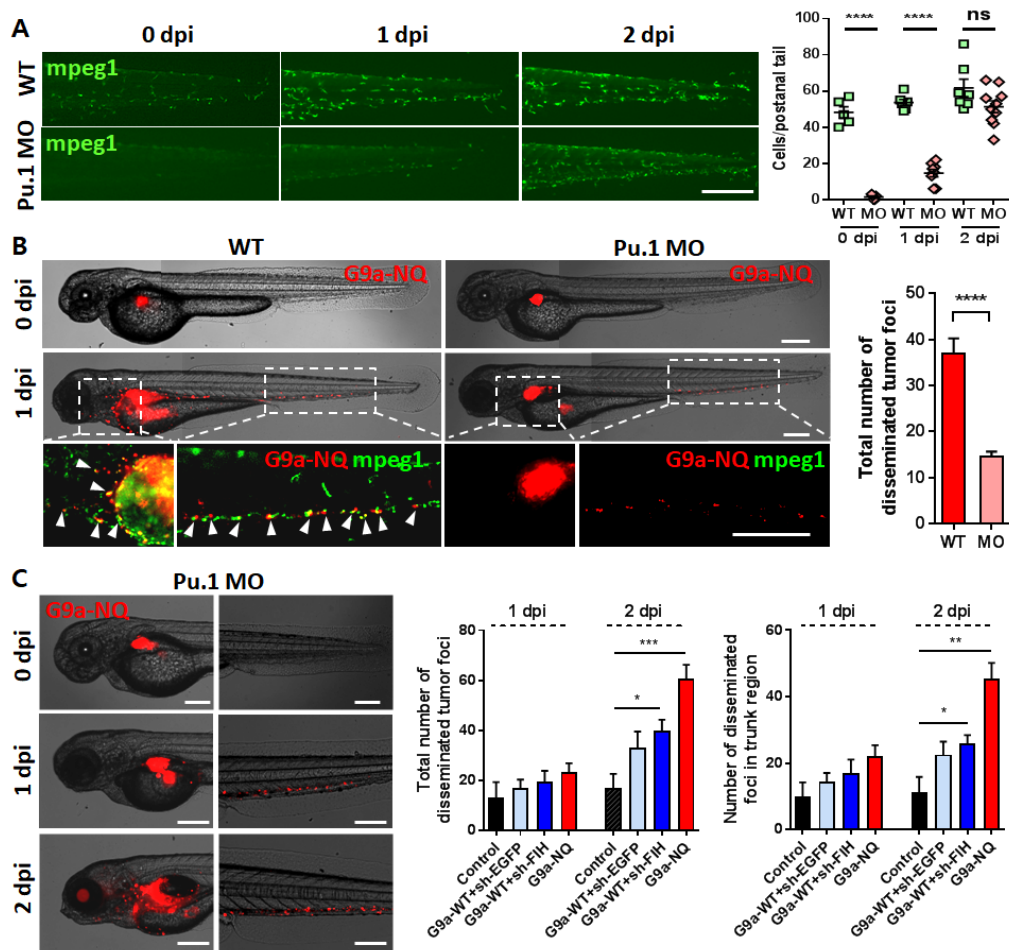
`

Figure 8. Myeloid cells depletion reduces metastasis of SKOV−3 cells. (A) Quantification of macrophages in the region of postanal tail in Pu.1 MO−injected embryos. The macrophages (green) were identified as effectively depleted until 72 hpf by MO injection. (B) Suppression of metastasis of SKOV−3 G9a−NQ cells (red) in Pu.1 MO−injected Tg(*mpeg1*:dendra2) zebrafish embryos compared to the uninjected controls. White arrowheads point to disseminated and metastatic cancer cells. (C) Delayed onset of metastasis of SKOV−3 cells due to the delayed generation of macrophages in Pu.1 MO−injected embryos. Quantification of the total number of disseminated tumor foci and the number of disseminated tumor foci in the trunk region was

`

conducted. (n = 10~20 embryos/group). Data represent mean $\pm$ S.E.M. $**p <$

0.01 $***p < 0.001$, $****p < 0.0001$ by Student's t-test. Scale bar; 250 μm.

`
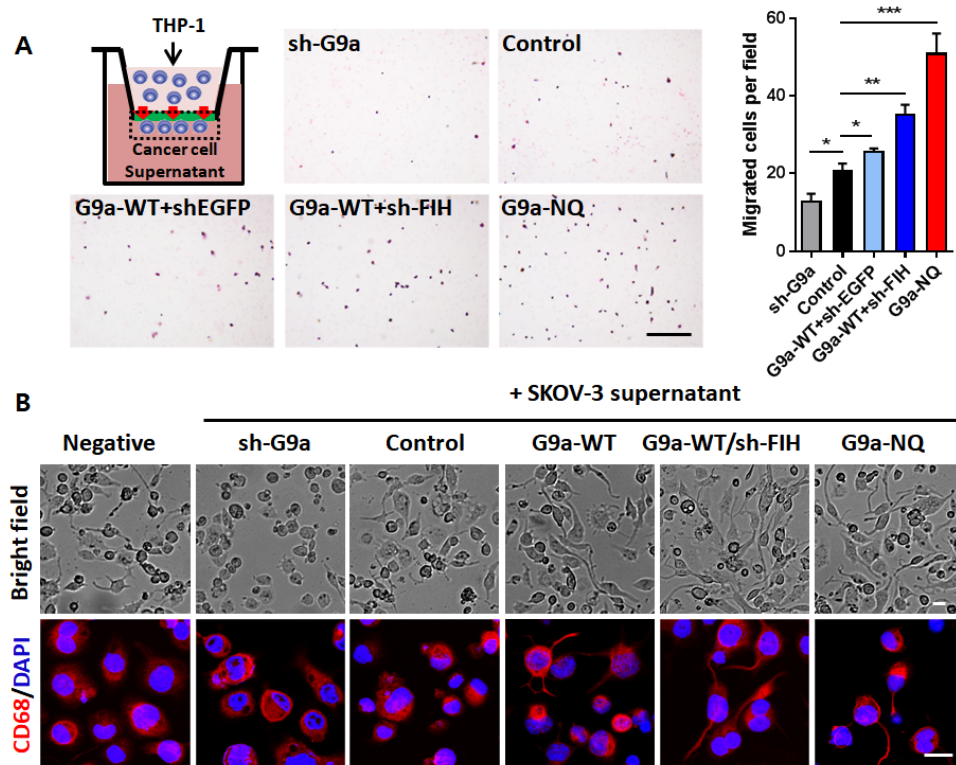
Figure 9. FIH-G9a axis promotes recruitment and differentiation of THP-1 monocytes. (A) Transwell migration assay using THP-1 monocytes towards supernatants obtained from different SKOV-3 cells. Magnification, × 200. Data represent mean ± S.E.M. n = 5 independent experiments. $*p < 0.05$, $***p < 0.001$ by Student's t-test. Scale bar; 200 μm. (B) Representative images of THP-1 macrophages stimulated with supernatants of different SKOV-3 cells for 3 days, and the fluorescence images of CD68 (red) and the nuclei (DAPI, blue) of supernatant-treated THP-1 macrophage. Scale bar; 20 μm

`
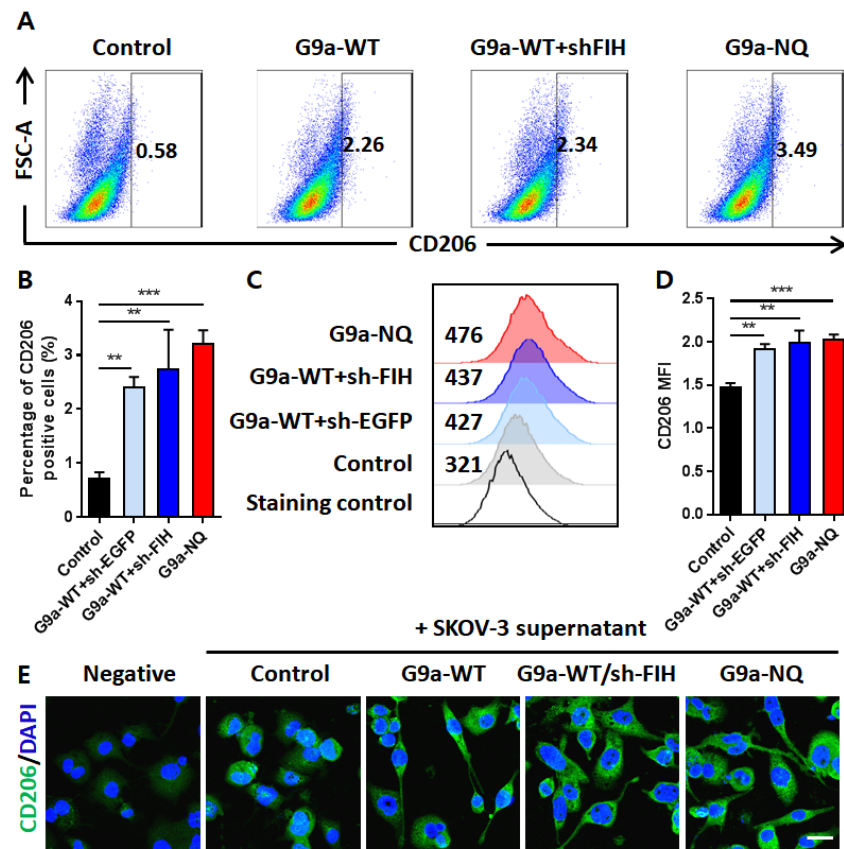
Figure 10. FIH-G9a axis upregulates CD206 expression in THP-1 macrophages. (A-E) Expression of CD206 in THP-1 macrophages stimulated with supernatants of different SKOV-3 cells for 3 days. The percentage of CD206 positive population (A, B) and the histograms (C, D) were measured by FACS analysis. n = 5. Data represent mean ± S.E.M. **$p < 0.01$ ***$p < 0.001$. The histograms are representatives of five independent experiments. Numerical values denote the mean fluorescence intensity (MFI). Immunofluorescence images showing CD206 expression in supernatant-treated THP-1 macrophages were also identified (E). Scale bar; 25 μm

`
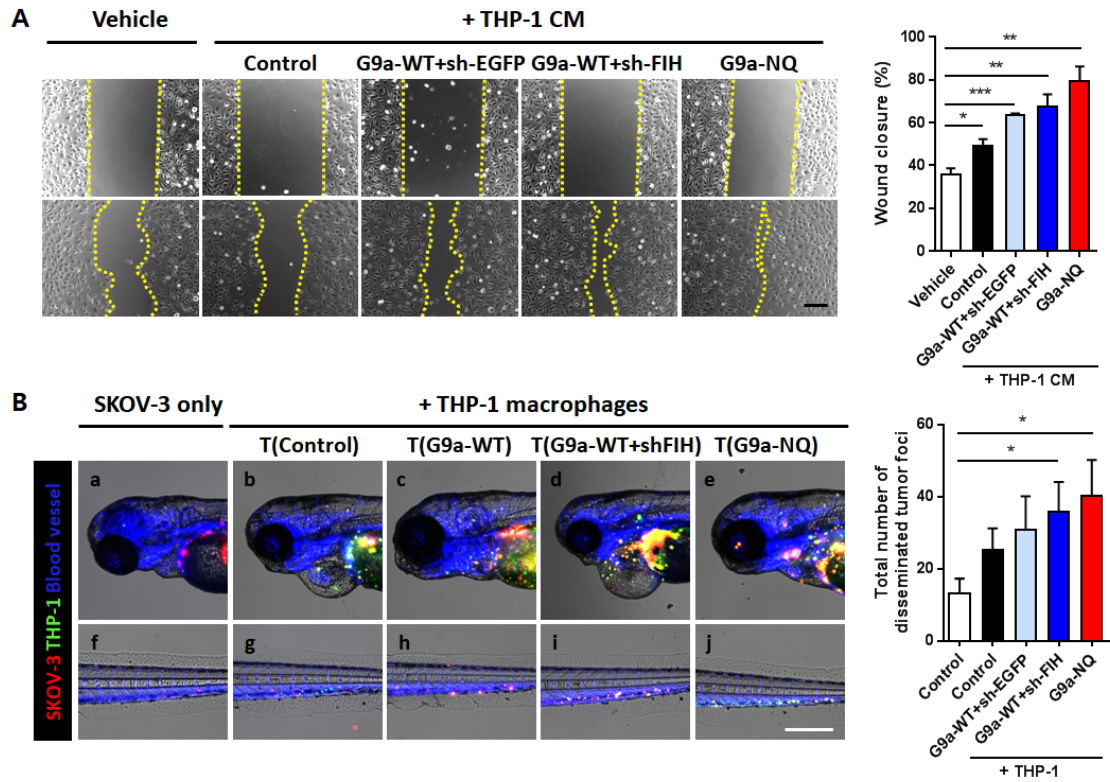
Figure 11. Activated THP-1 macrophages facilitate metastasis of SKOV-3 control cells. (A) Wound scratch assay showing increased motility in SKOV-3 control cells in response to the THP-1 CM. Scratches were photographed immediately (time 0) and at 6 h. Scale bar; 200 μm. (B) Representative fluorescence images of coimplantation experiments of SKOV-3 control cells and THP-1 macrophages stimulated with different supernatants of SKOV-3 cells for 3 days. The mixture of cells was coimplanted into PVS of each embryo. Quantification of the total number of the disseminated tumor foci in zebrafish embryos implanted with SKOV-3 control cells in combination with THP-1 macrophages was analyzed at 1 day after coimplantation. (n = 13~22 embryos/group). Scale bar; 250 μm. Data represent mean $\pm$ S.E.M. $*p <$ 0.05, $**p < 0.01$ $***p < 0.001$.

`
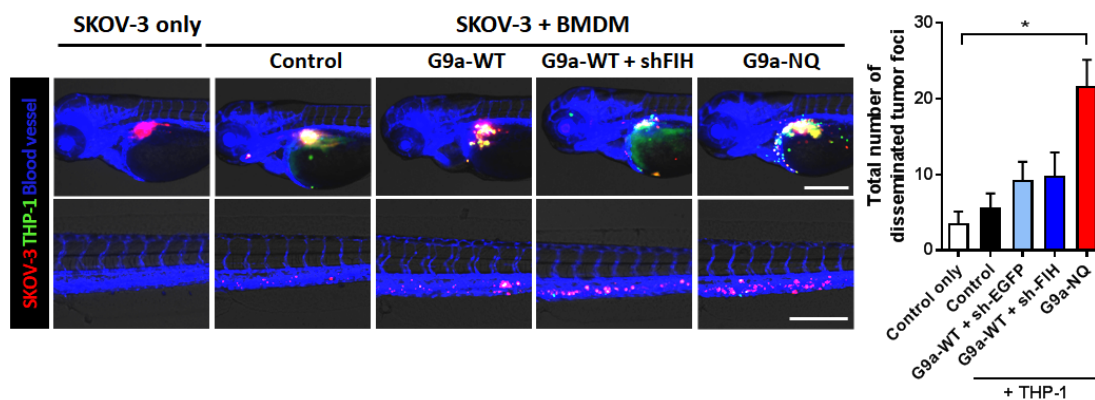
Figure 12. Activated mouse bone marrow-derived macrophages (BMDM) facilitate metastasis of SKOV-3 control cells. Representative fluorescence images of coimplantation experiments of SKOV-3 control cells and BMDM stimulated with different supernatants of SKOV-3 cells for 3 days. After removing zebrafish macrophages using 1mM Pu.1 MO, the mixture of cells was coimplanted into PVS of each embryo. Quantification of the total number of the disseminated tumor foci in zebrafish embryos implanted with SKOV-3 control cells in combination with THP-1 macrophages was analyzed at 1 day after coimplantation. (n = 5~14 embryos/group). Scale bar; 250 μm. Data represent mean $\pm$ S.E.M. $*p < 0.05$.
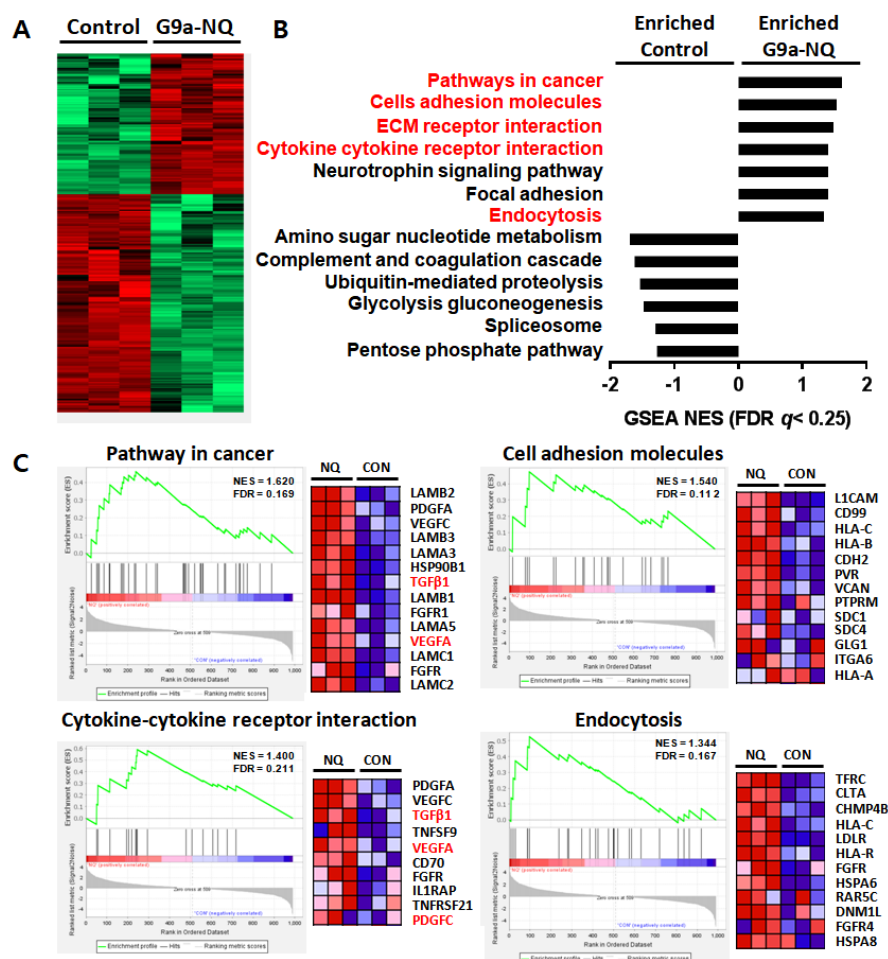
Figure 13. Differential protein secretome analysis in SKOV−3 control and NQ cells. (A) Heatmap displaying the expression of differentially secreted proteins identified from the nano LC−MS/MS analysis. The color scale illustrates the relative expression level of each protein across the 3 biological replicates in each experimental group; red and green indicate higher and lower expression compared to the median expression value (black), respectively. The color intensity indicates the degree of protein up− or downregulation. (B) Gene set enrichment analysis (GSEA) based on the latest MSigDB database for each collection. (C) GSEA plots and heat maps of the most enriched proteins between groups that strongly contributed to pathway enrichment

scores （ES） in gene set enrichment algorithm. NES, normalized enrichment score; FDR, false discovery rate.

`
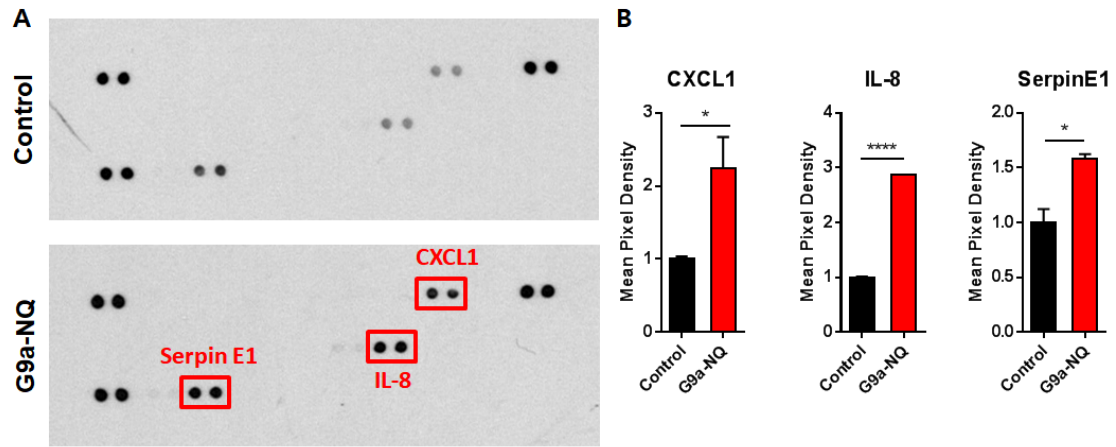
Figure 14. Human cytokine profile changes in SKOV-3 control and NQ cells. (A) Images of human cytokine antibody array that were assayed with conditioned medium obtained from SKOV-3 control and NQ cells. The signals of CXCL1, SerpinE1, and IL-8 were labeled with rectangle red boxes. (B) Quantification of cytokine and chemokine levels measured by the cytokine antibody array analyses. Each cytokine or chemokine spot on the blots in (A) was quantitated using Image J software. Data represent mean ± S.E.M. $*p < 0.05$, $****p < 0.0001$ by Student's t-test.

`
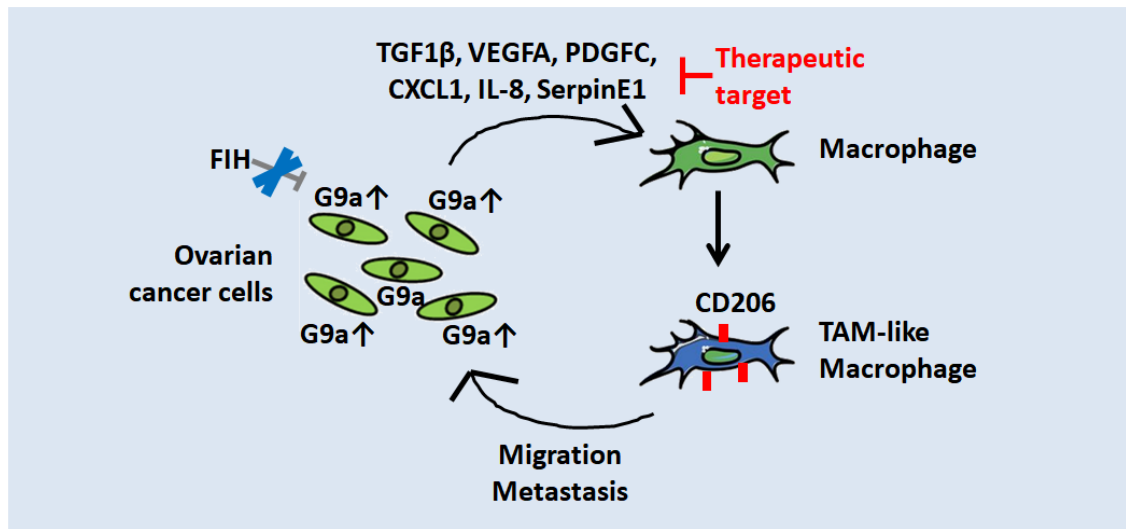
Figure 15. A proposed mechanism of FIH−G9a axis−induced macrophage activation and metastasis in ovarian cancer. G9a overexpression in ovarian cancer cells results in increase of pro−tumorigenic and pro−metastatic cytokines including TGF1β, VEGFA, PDGFC, CXCL1, IL−8, and SerpinE1. Then, monocyte recruitment as well as the expression of CD206 is upregulated by FIH−G9a axis. Reciprocally, activated macrophages enhance cancer cell migration and metastasis, forming a positive feedback loop.

`

7.4. DISCUSSION

For the first time, this study showed that ovarian cancer cells that modulated the expression of FIH−G9a axis secrete pro−tumorigenic and pro−metastatic cytokines, including TGFβ1, VEGFA, and PDGFC, to recruit monocytes and activate macrophages. Activated macrophages potentiate mobility and metastasis of cancer cells, forming a positive feedback loop. In addition, I clearly showed the critical role of macrophages during early cancer dissemination, suggesting that targeting of monocyte recruitment and macrophage activation could constitute a promising therapeutic strategy for hypoxia−induced metastasis.

FIH−dependent regulation of G9a has been reported to alter the expression of various genes [99]. Under normoxic conditions, FIH hydroxylates G9a, thus inhibiting methylation of H3K9 to activate gene transcription. Under hypoxia, however, G9a escapes from hydroxylation, leading to the generation of H3K9me2/me3 marks and epigenetic repression of the genes involved. Cell adhesion molecules, tumor suppressor genes, and metastasis suppressor genes have been reported to be methylated by G9a under hypoxic conditions, exacerbating tumor growth and metastasis [96, 99, 113]. Recently, G9a was found to be critical in silencing pro−inflammatory cytokines including TNF in breast cancer cells [114]. Similarly, this study also demonstrated that expression of anti−inflammatory cytokines, such as TGFβ and VEGFA, was elevated in G9a overexpressed ovarian cancer cells, implying that G9a serves to silence the expression of pro−inflammatory cytokines (Figure 13). These

`

findings strongly suggest that FIH-G9a is involved in the cytokine production, although the exact mechanism remains to be elucidated.

Infiltrated massively in hypoxic/necrotic regions within tumors, macrophages also respond quickly to hypoxia [115]. In response to the low oxygen tensions, macrophages have been reported to upregulate the potent pro-angiogenic-, pro-invasive-, and immunosuppressive factors, such as VEGF, fibroblast growth factor 2 (FGF2), matrix metalloproteinase (MMP)-7, TNFα, inducible NO synthase (iNOS), IL-10, and PGE$_2$, via upregulation of HIF1α [115-118]. In addition, the expression of CCR2, CCR5, and neuropilin-1 (NRP1) in TAMs was identified to be markedly reduced, leading them to be immobilized and trapped within the hypoxic niche [119-121]. Although it is not yet known whether the FIH-G9a axis is also involved in those hypoxia-driven gene expression changes in macrophages, it is presumed to play a key role when considering the previous reports that demonstrated epigenetic gene regulation during macrophage polarization [122]. Future research will be pursued in order to delineate the precise epigenetic mechanism of macrophage activation in terms of the hypoxic microenvironment.

Cancer cell intravasation is a rate-limiting step in metastasis that determines the number of circulating tumor cells and thus holds a high risk for the formation of secondary tumors [123, 124]. Previously, Harney *et al.* reported that direct contact between perivascular CD206^{high}Tie2^{high}VEGFA^{high} macrophage, Mammalian-enabled (Mena) over-expressing tumor cell, and endothelial cell, forming Tumor MicroEnvironment of Metastasis (TMEM), facilitated tumor cell intravasation and metastasis [125]. Cancer cells were identified as easily intravasated when macrophages were present and in direct

`

contact with these cells [126]. In addition, TGFβ secreted by cancer cells has been reported to upregulate CXCR4 expression in monocytes, while CXCL12 expressed by perivascular fibroblasts attracted these motile TAMs toward the blood vessels, bringing motile cancer cells with them [127]. In accordance with these previous results, I also observed macrophage-associated intravasation (Figure 2C) and dissemination (Figure 3C-G), and surprisingly, these processes were FIH-G9a axis dependent. Based on the secretome results obtained in this study showing increased levels of TGFβ1 and VEGFA (Figure 13), it is likely that the FIH-G9a axis of cancer cells facilitates macrophage-medicated intravasation of cancer cells, although precise experimental demonstration needs to be performed. The FIH-G9a axis of ovarian cancer cells seems to be an upstream regulator triggering macrophages to develop into perivascular macrophages, guiding them to endothelial cells.

Taken together, the results presented provide mechanistic insights into the role of the FIH-G9a signaling axis of cancer cells in facilitating cancer metastasis, which was revealed by investigating the interaction with TAMs. These findings would be a steppingstone towards an improved understanding of the early metastatic process. Based on a reliable model, it is expected that new therapeutic drugs able to block cancer intravasation and metastasis could potentially be developed by targeting associated macrophages.

`

8. REFERENCES

1.	S, G., *The Microenvironment of Chronic Disease.* Integrative and Functional Medical Nutrition Therapy, 2020.

2.	Pottier, C., et al., *The importance of the tumor microenvironment in the therapeutic management of cancer.* Expert Rev Anticancer Ther, 2015. **15**(8): p. 943-54.

3.	Kim, H., et al., *Macrophages-Triggered Sequential Remodeling of Endothelium-Interstitial Matrix to Form Pre-Metastatic Niche in Microfluidic Tumor Microenvironment.* Adv Sci (Weinh), 2019. **6**(11): p. 1900195.

4.	Murray, P.J., et al., *Macrophage activation and polarization: nomenclature and experimental guidelines.* Immunity, 2014. **41**(1): p. 14-20.

5.	Gordon, S., A. Pluddemann, and F. Martinez Estrada, *Macrophage heterogeneity in tissues: phenotypic diversity and functions.* Immunol Rev, 2014. **262**(1): p. 36-55.

6.	Boulton, M. and P. Dayhaw-Barker, *The role of the retinal pigment epithelium: topographical variation and ageing changes.* Eye (Lond), 2001. **15**(Pt 3): p. 384-9.

7.	Rizzolo, L.J., *Barrier properties of cultured retinal pigment epithelium.* Exp Eye Res, 2014. **126**: p. 16-26.

8.	Hurley, J.B., K.J. Lindsay, and J. Du, *Glucose, lactate, and shuttling of metabolites in vertebrate retinas.* J Neurosci Res, 2015. **93**(7): p. 1079-92.

9.	Mochizuki, M., S. Sugita, and K. Kamoi, *Immunological homeostasis of the eye.* Prog Retin Eye Res, 2013. **33**: p. 10-27.

10.	Horie, S., et al., *Human retinal pigment epithelium-induced CD4+CD25+ regulatory T cells suppress activation of intraocular effector T cells.* Clin Immunol, 2010. **136**(1): p. 83-95.

11.	Jager, R.D., W.F. Mieler, and J.W. Miller, *Age-related macular degeneration.* N Engl J Med, 2008. **358**(24): p. 2606-17.

`

12. Sparrow, J.R., D. Hicks, and C.P. Hamel, *The retinal pigment epithelium in health and disease.* Curr Mol Med, 2010. **10**(9): p. 802-23.

13. Xu, H., M. Chen, and J.V. Forrester, *Para-inflammation in the aging retina.* Prog Retin Eye Res, 2009. **28**(5): p. 348-68.

14. Wang, Y., et al., *NLRP3 Upregulation in Retinal Pigment Epithelium in Age-Related Macular Degeneration.* Int J Mol Sci, 2016. **17**(1).

15. Kauppinen, A., et al., *Inflammation and its role in age-related macular degeneration.* Cell Mol Life Sci, 2016. **73**(9): p. 1765-86.

16. Ambati, J., J.P. Atkinson, and B.D. Gelfand, *Immunology of age-related macular degeneration.* Nat Rev Immunol, 2013. **13**(6): p. 438-51.

17. Ambati, J. and B.J. Fowler, *Mechanisms of age-related macular degeneration.* Neuron, 2012. **75**(1): p. 26-39.

18. Stefansson, E., A. Geirsdottir, and H. Sigurdsson, *Metabolic physiology in age related macular degeneration.* Prog Retin Eye Res, 2011. **30**(1): p. 72-80.

19. Osborn, M.P., et al., *Metabolome-wide association study of neovascular age-related macular degeneration.* PLoS One, 2013. **8**(8): p. e72737.

20. Yokosako, K., et al., *Glycolysis in patients with age-related macular degeneration.* Open Ophthalmol J, 2014. **8**: p. 39-47.

21. Orban, T., et al., *Serum levels of lipid metabolites in age-related macular degeneration.* FASEB J, 2015. **29**(11): p. 4579-88.

22. Lains, I., et al., *Human plasma metabolomics in age-related macular degeneration (AMD) using nuclear magnetic resonance spectroscopy.* PLoS One, 2017. **12**(5): p. e0177749.

23. Mertins, P., et al., *Reproducible workflow for multiplexed deep-scale proteome and phosphoproteome analysis of tumor tissues by liquid chromatography-mass spectrometry.* Nat Protoc, 2018. **13**(7): p. 1632-1661.

24. Hasan, M., et al., *Quantitative Proteome Analysis of Brain Subregions and Spinal Cord from Experimental Autoimmune Encephalomyelitis Mice by TMT-Based Mass Spectrometry.* Proteomics, 2019. **19**(5): p. e1800355.

`

25. Kim, D.K., et al., *Deep proteome profiling of the hippocampus in the 5XFAD mouse model reveals biological process alterations and a novel biomarker of Alzheimer's disease.* Exp Mol Med, 2019. **51**(11): p. 1-17.

26. Wisniewski, J.R. and F.Z. Gaugaz, *Fast and sensitive total protein and Peptide assays for proteomic analysis.* Anal Chem, 2015. **87**(8): p. 4110-6.

27. Jin, M.S., et al., *Integrated Multi-Omic Analyses Support Distinguishing Secretory Carcinoma of the Breast from Basal-Like Triple-Negative Breast Cancer.* Proteomics Clin Appl, 2018. **12**(5): p. e1700125.

28. Humphrey, S.J., et al., *High-throughput and high-sensitivity phosphoproteomics with the EasyPhos platform.* Nat Protoc, 2018. **13**(9): p. 1897-1916.

29. Parkin, M., et al., *[Incidence of cancer in children throughout the world].* Pediatrie, 1989. **44**(9): p. 725-36.

30. Perez-Riverol, Y., et al., *The PRIDE database and related tools and resources in 2019: improving support for quantification data.* Nucleic Acids Res, 2019. **47**(D1): p. D442-D450.

31. Tyanova, S., et al., *The Perseus computational platform for comprehensive analysis of (prote)omics data.* Nat Methods, 2016. **13**(9): p. 731-40.

32. Bindea, G., et al., *ClueGO: a Cytoscape plug-in to decipher functionally grouped gene ontology and pathway annotation networks.* Bioinformatics, 2009. **25**(8): p. 1091-3.

33. Shannon, P., et al., *Cytoscape: a software environment for integrated models of biomolecular interaction networks.* Genome Res, 2003. **13**(11): p. 2498-504.

34. Szklarczyk, D., et al., *The STRING database in 2017: quality-controlled protein-protein association networks, made broadly accessible.* Nucleic Acids Res, 2017. **45**(D1): p. D362-D368.

35. Kruger, N.J., M.A. Troncoso-Ponce, and R.G. Ratcliffe, *1H NMR metabolite fingerprinting and metabolomic analysis of perchloric acid extracts from plant tissues.* Nat Protoc, 2008. **3**(6): p. 1001-12.

`

36. Ramos, H., P. Shannon, and R. Aebersold, *The protein information and property explorer: an easy-to-use, rich-client web application for the management and functional analysis of proteomic data.* Bioinformatics, 2008. **24**(18): p. 2110-1.

37. Yi, X., et al., *Vascular endothelial growth factor expression in choroidal neovascularization in rats.* Graefes Arch Clin Exp Ophthalmol, 1997. **235**(5): p. 313-9.

38. Handa, J.T., et al., *A systems biology approach towards understanding and treating non-neovascular age-related macular degeneration.* Nat Commun, 2019. **10**(1): p. 3347.

39. Bermudez, V., et al., *Lipopolysaccharide-Induced Autophagy Mediates Retinal Pigment Epithelium Cells Survival. Modulation by the Phospholipase D Pathway.* Front Cell Neurosci, 2019. **13**: p. 154.

40. Ozal, S.A., et al., *Esculetin Protects Human Retinal Pigment Epithelial Cells from Lipopolysaccharide-induced Inflammation and Cell Death.* Curr Eye Res, 2018. **43**(9): p. 1169-1176.

41. Gao, J., et al., *NLRP3 inflammasome: activation and regulation in age-related macular degeneration.* Mediators Inflamm, 2015. **2015**: p. 690243.

42. Paeng, S.H., et al., *YCG063 inhibits Pseudomonas aeruginosa LPS-induced inflammation in human retinal pigment epithelial cells through the TLR2-mediated AKT/NF-kappaB pathway and ROS-independent pathways.* Int J Mol Med, 2015. **36**(3): p. 808-16.

43. Zhu, Y., et al., *C5a and toll-like receptor 4 crosstalk in retinal pigment epithelial cells.* Mol Vis, 2015. **21**: p. 1122-9.

44. Zou, X.L., et al., *Protection of tight junction between RPE cells with tissue factor targeting peptide.* Int J Ophthalmol, 2018. **11**(10): p. 1594-1599.

45. Leung, K.W., C.J. Barnstable, and J. Tombran-Tink, *Bacterial endotoxin activates retinal pigment epithelial cells and induces their degeneration through IL-6 and IL-8 autocrine signaling.* Mol Immunol, 2009. **46**(7): p. 1374-86.

`

46. Tao, L., et al., *Angiotensin-converting enzyme 2 activator diminazene aceturate prevents lipopolysaccharide-induced inflammation by inhibiting MAPK and NF-kappaB pathways in human retinal pigment epithelium.* J Neuroinflammation, 2016. **13**: p. 35.

47. Dridi, S., et al., *ERK1/2 activation is a therapeutic target in age-related macular degeneration.* Proc Natl Acad Sci U S A, 2012. **109**(34): p. 13781-6.

48. Zhou, T., et al., *The pathogenic role of the canonical Wnt pathway in age-related macular degeneration.* Invest Ophthalmol Vis Sci, 2010. **51**(9): p. 4371-9.

49. Tuo, J., et al., *Wnt signaling in age-related macular degeneration: human macular tissue and mouse model.* J Transl Med, 2015. **13**: p. 330.

50. Ma, B. and M.O. Hottiger, *Crosstalk between Wnt/beta-Catenin and NF-kappaB Signaling Pathway during Inflammation.* Front Immunol, 2016. **7**: p. 378.

51. Zhao, J., et al., *AMP-activated protein kinase (AMPK) cross-talks with canonical Wnt signaling via phosphorylation of beta-catenin at Ser 552.* Biochem Biophys Res Commun, 2010. **395**(1): p. 146-51.

52. Vallee, A., et al., *Aerobic Glycolysis Hypothesis Through WNT/Beta-Catenin Pathway in Exudative Age-Related Macular Degeneration.* J Mol Neurosci, 2017. **62**(3-4): p. 368-379.

53. Fan, Q., et al., *Autophagy promotes metastasis and glycolysis by upregulating MCT1 expression and Wnt/beta-catenin signaling pathway activation in hepatocellular carcinoma cells.* J Exp Clin Cancer Res, 2018. **37**(1): p. 9.

54. Vallee, A., et al., *Circadian Rhythms in Exudative Age-Related Macular Degeneration: The Key Role of the Canonical WNT/beta-Catenin Pathway.* Int J Mol Sci, 2020. **21**(3).

55. Zhao, C., et al., *mTOR-mediated dedifferentiation of the retinal pigment epithelium initiates photoreceptor degeneration in mice.* J Clin Invest, 2011. **121**(1): p. 369-83.

`

56. Hu, Y., et al., *Pathogenic role of the Wnt signaling pathway activation in laser-induced choroidal neovascularization.* Invest Ophthalmol Vis Sci, 2013. **54**(1): p. 141-54.

57. Luu, J. and K. Palczewski, *Human aging and disease: Lessons from age-related macular degeneration.* Proc Natl Acad Sci U S A, 2018. **115**(12): p. 2866-2872.

58. Fisher, C.R. and D.A. Ferrington, *Perspective on AMD Pathobiology: A Bioenergetic Crisis in the RPE.* Invest Ophthalmol Vis Sci, 2018. **59**(4): p. AMD41-AMD47.

59. Adijanto, J. and N.J. Philp, *Cultured primary human fetal retinal pigment epithelium (hfRPE) as a model for evaluating RPE metabolism.* Exp Eye Res, 2014. **126**: p. 77-84.

60. Leveillard, T., N.J. Philp, and F. Sennlaub, *Is Retinal Metabolic Dysfunction at the Center of the Pathogenesis of Age-related Macular Degeneration?* Int J Mol Sci, 2019. **20**(3).

61. Xu, L., et al., *Stimulation of AMPK prevents degeneration of photoreceptors and the retinal pigment epithelium.* Proc Natl Acad Sci U S A, 2018. **115**(41): p. 10475-10480.

62. Kokoszka, J.E., et al., *Increased mitochondrial oxidative stress in the Sod2 (+/-) mouse results in the age-related decline of mitochondrial function culminating in increased apoptosis.* Proc Natl Acad Sci U S A, 2001. **98**(5): p. 2278-83.

63. Brown, E.E., et al., *Mitochondrial oxidative stress in the retinal pigment epithelium (RPE) led to metabolic dysfunction in both the RPE and retinal photoreceptors.* Redox Biol, 2019. **24**: p. 101201.

64. Drane, P., et al., *Reciprocal down-regulation of p53 and SOD2 gene expression-implication in p53 mediated apoptosis.* Oncogene, 2001. **20**(4): p. 430-9.

65. Winkler, B.S., et al., *Cultured retinal neuronal cells and Muller cells both show net production of lactate.* Neurochem Int, 2004. **45**(2-3): p. 311-20.

66. Zhu, D., J. Zhou, and X. Xu, *Influence of lactic acid on differential expression of vascular endothelial growth factor and pigment*

`

epithelium-derived factor in explants of rat retina. Curr Eye Res, 2012. **37**(11): p. 1025-9.

67. Hermansen, L. and I. Stensvold, *Production and removal of lactate during exercise in man.* Acta Physiol Scand, 1972. **86**(2): p. 191-201.

68. Murakami, N., et al., *G2A is a proton-sensing G-protein-coupled receptor antagonized by lysophosphatidylcholine.* J Biol Chem, 2004. **279**(41): p. 42484-91.

69. Kabarowski, J.H., *G2A and LPC: regulatory functions in immunity.* Prostaglandins Other Lipid Mediat, 2009. **89**(3-4): p. 73-81.

70. Bolick, D.T., et al., *G2A deficiency in mice promotes macrophage activation and atherosclerosis.* Circ Res, 2009. **104**(3): p. 318-27.

71. Chen, P., et al., *Gpr132 sensing of lactate mediates tumor-macrophage interplay to promote breast cancer metastasis.* Proc Natl Acad Sci U S A, 2017. **114**(3): p. 580-585.

72. Colegio, O.R., et al., *Functional polarization of tumour-associated macrophages by tumour-derived lactic acid.* Nature, 2014. **513**(7519): p. 559-63.

73. Tsutsumi, C., et al., *The critical role of ocular-infiltrating macrophages in the development of choroidal neovascularization.* J Leukoc Biol, 2003. **74**(1): p. 25-32.

74. Krause, T.A., et al., *VEGF-production by CCR2-dependent macrophages contributes to laser-induced choroidal neovascularization.* PLoS One, 2014. **9**(4): p. e94313.

75. Xie, P., et al., *Suppression and regression of choroidal neovascularization in mice by a novel CCR2 antagonist, INCB3344.* PLoS One, 2011. **6**(12): p. e28933.

76. Kim, S.J., et al., *Intravitreal TSG-6 suppresses laser-induced choroidal neovascularization by inhibiting CCR2+ monocyte recruitment.* Sci Rep, 2015. **5**: p. 11872.

77. Espinosa-Heidmann, D.G., et al., *Macrophage depletion diminishes lesion size and severity in experimental choroidal neovascularization.* Invest Ophthalmol Vis Sci, 2003. **44**(8): p. 3586-92.

`

78. Sakurai, E., et al., *Macrophage depletion inhibits experimental choroidal neovascularization.* Invest Ophthalmol Vis Sci, 2003. **44**(8): p. 3578-85.

79. Gragoudas, E.S., et al., *Pegaptanib for neovascular age-related macular degeneration.* N Engl J Med, 2004. **351**(27): p. 2805-16.

80. Rosenfeld, P.J., et al., *Ranibizumab for neovascular age-related macular degeneration.* N Engl J Med, 2006. **355**(14): p. 1419-31.

81. Enslow, R., et al., *Association of Anti-VEGF Injections with Progression of Geographic Atrophy.* Ophthalmol Eye Dis, 2016. **8**: p. 31-2.

82. He, L. and A.G. Marneros, *Doxycycline inhibits polarization of macrophages to the proangiogenic M2-type and subsequent neovascularization.* J Biol Chem, 2014. **289**(12): p. 8019-28.

83. Zandi, S., et al., *ROCK-isoform-specific polarization of macrophages associated with age-related macular degeneration.* Cell Rep, 2015. **10**(7): p. 1173-86.

84. Sonveaux, P., et al., *Targeting the lactate transporter MCT1 in endothelial cells inhibits lactate-induced HIF-1 activation and tumor angiogenesis.* PLoS One, 2012. **7**(3): p. e33418.

85. Ruan, G.X. and A. Kazlauskas, *Lactate engages receptor tyrosine kinases Axl, Tie2, and vascular endothelial growth factor receptor 2 to activate phosphoinositide 3-kinase/Akt and promote angiogenesis.* J Biol Chem, 2013. **288**(29): p. 21161-72.

86. Belli, C., et al., *Targeting the microenvironment in solid tumors.* Cancer Treat Rev, 2018. **65**: p. 22-32.

87. Afik, R., et al., *Tumor macrophages are pivotal constructors of tumor collagenous matrix.* J Exp Med, 2016. **213**(11): p. 2315-2331.

88. Luo, Y., et al., *Targeting tumor-associated macrophages as a novel strategy against breast cancer.* J Clin Invest, 2006. **116**(8): p. 2132-2141.

89. Noy, R. and J.W. Pollard, *Tumor-associated macrophages: from mechanisms to therapy.* Immunity, 2014. **41**(1): p. 49-61.

90. Cao, Y., *Opinion: emerging mechanisms of tumour lymphangiogenesis and lymphatic metastasis.* Nat Rev Cancer, 2005. **5**(9): p. 735-43.

`

91.   Wang, J., et al., *Novel mechanism of macrophage-mediated metastasis revealed in a zebrafish model of tumor development.* Cancer Res, 2015. **75**(2): p. 306-15.

92.   Tachibana, M., et al., *Histone methyltransferases G9a and GLP form heteromeric complexes and are both crucial for methylation of euchromatin at H3-K9.* Genes Dev, 2005. **19**(7): p. 815-26.

93.   Rai, K., et al., *Dnmt3 and G9a cooperate for tissue-specific development in zebrafish.* J Biol Chem, 2010. **285**(6): p. 4110-21.

94.   Shinkai, Y. and M. Tachibana, *H3K9 methyltransferase G9a and the related molecule GLP.* Genes Dev, 2011. **25**(8): p. 781-8.

95.   Casciello, F., et al., *Functional Role of G9a Histone Methyltransferase in Cancer.* Front Immunol, 2015. **6**: p. 487.

96.   Chen, M.W., et al., *H3K9 histone methyltransferase G9a promotes lung cancer invasion and metastasis by silencing the cell adhesion molecule Ep-CAM.* Cancer Res, 2010. **70**(20): p. 7830-40.

97.   Zhang, K., et al., *Targeting histone methyltransferase G9a inhibits growth and Wnt signaling pathway by epigenetically regulating HP1alpha and APC2 gene expression in non-small cell lung cancer.* Mol Cancer, 2018. **17**(1): p. 153.

98.   Segovia, C., et al., *Inhibition of a G9a/DNMT network triggers immune-mediated bladder cancer regression.* Nat Med, 2019. **25**(7): p. 1073-1081.

99.   Kang, J., et al., *FIH Is an Oxygen Sensor in Ovarian Cancer for G9a/GLP-Driven Epigenetic Regulation of Metastasis-Related Genes.* Cancer Res, 2018. **78**(5): p. 1184-1199.

100.   Liu, C., et al., *A Zebrafish Model Discovers a Novel Mechanism of Stromal Fibroblast-Mediated Cancer Metastasis.* Clin Cancer Res, 2017. **23**(16): p. 4769-4779.

101.   Veinotte, C.J., G. Dellaire, and J.N. Berman, *Hooking the big one: the potential of zebrafish xenotransplantation to reform cancer drug screening in the genomic era.* Dis Model Mech, 2014. **7**(7): p. 745-54.

`

102. Rhodes, J., et al., *Interplay of pu.1 and gata1 determines myelo-erythroid progenitor cell fate in zebrafish.* Dev Cell, 2005. **8**(1): p. 97-108.

103. He, S., et al., *Neutrophil-mediated experimental metastasis is enhanced by VEGFR inhibition in a zebrafish xenograft model.* J Pathol, 2012. **227**(4): p. 431-45.

104. Bill, B.R., et al., *A primer for morpholino use in zebrafish.* Zebrafish, 2009. **6**(1): p. 69-77.

105. Han, D., et al., *Proteomic analysis of mouse astrocytes and their secretome by a combination of FASP and StageTip-based, high pH, reversed-phase fractionation.* Proteomics, 2014. **14**(13-14): p. 1604-9.

106. Lee, H., et al., *Quantitative Proteomic Analysis Identifies AHNAK (Neuroblast Differentiation-associated Protein AHNAK) as a Novel Candidate Biomarker for Bladder Urothelial Carcinoma Diagnosis by Liquid-based Cytology.* Mol Cell Proteomics, 2018. **17**(9): p. 1788-1802.

107. Stoletov, K., et al., *High-resolution imaging of the dynamic tumor cell vascular interface in transparent zebrafish.* Proc Natl Acad Sci U S A, 2007. **104**(44): p. 17406-11.

108. White, R.M., et al., *Transparent adult zebrafish as a tool for in vivo transplantation analysis.* Cell Stem Cell, 2008. **2**(2): p. 183-9.

109. Feng, Y. and P. Martin, *Imaging innate immune responses at tumour initiation: new insights from fish and flies.* Nat Rev Cancer, 2015. **15**(9): p. 556-62.

110. Roh-Johnson, M., et al., *Macrophage-Dependent Cytoplasmic Transfer during Melanoma Invasion In Vivo.* Dev Cell, 2017. **43**(5): p. 549-562 e6.

111. Garbis, S., G. Lubec, and M. Fountoulakis, *Limitations of current proteomics technologies.* J Chromatogr A, 2005. **1077**(1): p. 1-18.

112. De Boeck, A., et al., *Differential secretome analysis of cancer-associated fibroblasts and bone marrow-derived precursors to identify*

`

microenvironmental regulators of colon cancer progression.* Proteomics, 2013. **13**(2): p. 379-88.

113. Casciello, F., et al., *G9a drives hypoxia-mediated gene repression for breast cancer cell survival and tumorigenesis.* Proc Natl Acad Sci U S A, 2017. **114**(27): p. 7077-7082.

114. Nathaniel W. Mabe, S.E.W., Rachel Newcomb, Ryan C. Meingasner, Brittany A. Vilona, Chao-Chiehl Lin, Ryan Lupo, Jen-Tsan Chi, James V. Alvarez, *G9a promotes breast cancer recurrence through repression of a pro-inflammatory program.* BioRxiv preprint, 2020.

115. Murdoch, C., M. Muthana, and C.E. Lewis, *Hypoxia regulates macrophage functions in inflammation.* J Immunol, 2005. **175**(10): p. 6257-63.

116. Lewis, J.S., et al., *Expression of vascular endothelial growth factor by macrophages is up-regulated in poorly vascularized areas of breast carcinomas.* J Pathol, 2000. **192**(2): p. 150-8.

117. Burke, B., et al., *Hypoxia-induced gene expression in human macrophages: implications for ischemic tissues and hypoxia-regulated gene therapy.* Am J Pathol, 2003. **163**(4): p. 1233-43.

118. Lewis, C. and C. Murdoch, *Macrophage responses to hypoxia: implications for tumor progression and anti-cancer therapies.* Am J Pathol, 2005. **167**(3): p. 627-35.

119. Grimshaw, M.J. and F.R. Balkwill, *Inhibition of monocyte and macrophage chemotaxis by hypoxia and inflammation--a potential mechanism.* Eur J Immunol, 2001. **31**(2): p. 480-9.

120. Bosco, M.C., et al., *Hypoxia inhibits the expression of the CCR5 chemokine receptor in macrophages.* Cell Immunol, 2004. **228**(1): p. 1-7.

121. Sica, A., et al., *Defective expression of the monocyte chemotactic protein-1 receptor CCR2 in macrophages associated with human ovarian carcinoma.* J Immunol, 2000. **164**(2): p. 733-8.

122. de Groot, A.E. and K.J. Pienta, *Epigenetic control of macrophage polarization: implications for targeting tumor-associated macrophages.* Oncotarget, 2018. **9**(29): p. 20908-20927.

`

123. Nguyen, D.X., P.D. Bos, and J. Massague, *Metastasis: from dissemination to organ-specific colonization.* Nat Rev Cancer, 2009. **9**(4): p. 274-84.

124. Steeg, P.S., *Tumor metastasis: mechanistic insights and clinical challenges.* Nat Med, 2006. **12**(8): p. 895-904.

125. Harney, A.S., et al., *Real-Time Imaging Reveals Local, Transient Vascular Permeability, and Tumor Cell Intravasation Stimulated by TIE2hi Macrophage-Derived VEGFA.* Cancer Discov, 2015. **5**(9): p. 932-43.

126. Roh-Johnson, M., et al., *Macrophage contact induces RhoA GTPase signaling to trigger tumor cell intravasation.* Oncogene, 2014. **33**(33): p. 4203-12.

127. Arwert, E.N., et al., *A Unidirectional Transition from Migratory to Perivascular Macrophage Is Required for Tumor Cell Intravasation.* Cell Rep, 2018. **23**(5): p. 1239-1248.

`

9. 국문 초록

염증 및 종양 미세환경에 매우 높은 비율로 존재하는 큰포식세포는 병인 부위에 침윤하여 미세환경을 질병 진행에 우호적인 환경으로 조절한다. 큰포식세포는 모여들게 한 인자나 침윤한 부위의 미세환경에 반응하여 기능적으로 높은 다양성을 나타내기 때문에 질병 특이적 미세환경 맥락에서 큰포식세포를 분석하고 질병 치료를 위한 조절 전략을 세우는 것이 중요하다. 이러한 관점에서 본 연구에서는 눈의 염증질환인 맥락막 혈관신생증과 난소암에서 나타나는 미세환경 변화를 확인하고 그 질병 상황에 침윤한 큰포식세포의 특성을 미세환경 변화 측면에서 조사함으로써 효과적인 치료학적 접근법을 제시하고자 하였다. 첫 번째로, 망막상피세포에 과도한 염증이 가해지면 미토콘드리아 대사가 억제되고 그로 인해 당, 지질, 그리고 아미노산 대사에도 교란이 생기는 것을 관찰하였다. 이 결과와 일치하여 실제로 실험적으로 유도한 맥락막 혈관신생증 마우스의 망막상피세포 및 맥락막 층에서 정상 마우스보다 해당작용의 대사산물인 젖산이 높은 농도로 증가되어 있는 것이 확인되었다. 젖산은 맥락막 혈관신생부위에 침윤한 큰포식세포에 영향을 미쳐 큰포식세포의 혈관신생능력을 증가시키는데, 이러한 젖산의 영향을 받는 큰포식세포를 최초로 타겟팅함으로써 혈관신생이 감소됨을 실험적으로 증명하였다. 즉, 미세환경 내에 존재하는 대사체와 큰포식세포와의 연결고리를 표적으로 하는 전략이 치료학적으로 유효함을 제시하였다 (Chapter 1). 두 번째로, 저산소에 의한 종양 전이 증가 양상 및 미세환경과의 상호작용을 확인하기 위해 FIH-G9a axis의 발현을 인위적으로 조작한 난소암세포주를 이용하여 저산소에 의해 전이가 증가되는 때의 미세환경의 변화 및 종양미세환경 내 침윤한 큰포식세포와의 상호작용을 처음으로 관찰하였다. 제브라피쉬 종양 전이 모델을 이용하여 확인한 결과, FIH-G9a axis에 의해 단핵구의 침윤, 큰포식세포의 활성화가 증가하는 것이 관찰되었고 특히 초기 종양 전이 과정에서 큰포식세포가 종양세포 근처에서 긴밀히 상호작

`

용하는 것을 관찰하였다. 기전 분석을 위해 난소암 세포의 FIH-G9a axis 활성화에 따른 분비체 분석을 실시하여 종양의 성장과 전이를 돕는 역할을 하는 TGFβ1, VEGFA, 그리고 PDGFC와 같은 사이토카인이 유의적으로 증가되어 분비되는 것을 확인하였다. 본 연구는 제브라피쉬 종양 전이 모델을 이용하여 종양 전이 초기 과정에서 종양세포와 큰포식세포와의 사이에서 나타나는 상호작용이 초기 종양 전파에 중요함을 밝혔고, 미세환경에 의해 활성화되는 큰포식세포를 억제함으로써 종양의 혈관 내 유입을 감소시킬 수 있을 것으로 제시하였다 (Chapter 2).

결론적으로 본 논문은 눈의 염증에서 큰포식세포가 관여하는 대사체 조절을 처음으로 진행하였고, 종양 전이과정에서 저산소를 감지하는 FIH-G9a axis 활성화에 따른 큰포식세포의 종양전이 기전을 규명하여 새로운 치료학적 전략을 제시한 것에 의의가 있다. 본 연구의 결과는 향후 염증 질환 및 종양 미세환경에서 큰포식세포의 관련 기전 이해 및 치료학적 접근에 중요한 근거 자료로 사용될 수 있을 것으로 기대된다.

주요어 : 미세환경, 큰포식세포, 염증, 맥락막 혈관신생증, 난소암

학 번 : 2015-30482

`